PROCEEDINGS A

royalsocietypublishing.org/journal/rspa

Research

Article submitted to journal

Subject Areas:
Applied Mathematics, Mathematical Physics, Biomechanics

Keywords:
Homogenization, Darcy-Brinkman, Lymph Node

Effective governing equations for dual porosity Darcy-Brinkman systems subjected to inhomogeneous body forces and their application to the lymph node

A. Girelli [1], G. Giantesio [1,2], A. Musesti [1], R. Penta [3]

[1]Dipartimento di Matematica e Fisica “N. Tartaglia”, Università Cattolica del Sacro Cuore, Brescia, Italy.
[2]“Mathematics for Technology, Medicine & Biosciences", Università degli Studi di Ferrara, Italy.
[3]School of Mathematics and Statistics, University of Glasgow, Glasgow, UK.

We derive the homogenised governing equations for a double porosity system where the fluid flow within the individual compartments is governed by the coupling between the Darcy and the Darcy-Brinkman equations at the *microscale,* and are subjected to inhomogeneous body forces. The homogenised *macroscale* results are obtained by means of the asymptotic homogenization technique and read as a double Darcy differential model with mass exchange between phases. The role of the microstructure is encoded in the effective hydraulic conductivities which are obtained by solving periodic cell problems whose properties are illustrated and compared. We conclude by solving the new model by means of a semi-analytical approach under the assumption of azimuthal axisymmetry to model the movement of fluid within a lymph node.

Introduction

Flow of a Newtonian fluid inside a rigid porous matrix can be macroscopically described by Darcy’s law.

THE ROYAL SOCIETY PUBLISHING

The latter was formulated by Henry Darcy based on the results of experiments on the flow of water through beds of sand [1], and can be rigorously derived by a large variety of upscaling methods such as mixture theory and asymptotic homogenisation, see, e.g., [2] and [3,4], respectively. An alternative approach that describes the fluid flow of a Newtonian fluid inside a rigid porous matrix relies on the Darcy-Brinkman equation. The latter has been introduced by Brinkman adding the so called *Brinkman* term, that is, an additional viscous term to the classical Darcy equation [5], represented by a Laplacian weighted by an effective viscosity μ_e. This model has been used widely to analyze high-porosity porous media. In particular, the Darcy-Brinkman formulation allows us to specify the boundary conditions [6] and the interaction between a free-fluid region and a porous region [7], having a differential form similar to the Stokes' one. Despite its practical feedback, the Darcy-Brinkman equation is more complex and less straightforward to justify than Darcy's law via upscaling method such as homogenisation, see, e.g., [3,8,9], and is also computationally more demanding. Furthermore, the Darcy and Darcy-Brinkman equations possess very different differential structures.

In this manuscript, we derive a new macroscale model which is obtained by upscaling a system of partial differential equations resulting from the coupling between Darcy's and Darcy-Brinkman's models. This means that, while we are considering the interactions between two porous media, pore-scale inhomogeneities are already "smoothed out" from a geometrical viewpoint, and the upscaling process is performed by considering the interaction between the two phases at the mesoscale level. The two media are both considered intrinsically incompressible and subjected to inhomogeneous body forces, which can for example arise from the application of electromagnetic fields on e.g. magnetorheological fluids or electrolytes, see also [10]. We have also assumed that the two compartments are exchanging mass through their interface, which is modeled as a semi-permeable membrane. As a result, we obtain a double porosity macroscale model which is equipped with an effective source. This latter comprises contributions related to both the meso and macro scale variations of the prescribed body forces mediated by the properties of the mesoscale structure, as well as mass exchange terms involving the pressure jumps between the two compartments at the macroscale.

The derivation of the macroscopic equations related to this problem is as general as possible, so the model is applicable to a large variety of scenarios of interest involving multiscale fluid flow in porous media. However, the chief motivation driving the present study is the application of the results to fluid flow within a lymph node. The lymph node is an essential component of the immune and lymphatic system, playing a critical role in safeguarding the body against infection and disease. It accomplishes this by harboring lymphocytes, including B and T cells, which travel through the bloodstream and reside within the nodes. B cells are responsible for generating antibodies that specifically attach to antigens, thus initiating an immune response. When B cells are stimulated, they can transform into plasma cells, which secrete antibodies, or memory cells that provide defense in future encounters. Additionally, antigen-presenting cells, such as dendritic cells, capture and process antigens from various sources. These cells migrate to the lymph nodes, presenting the antigens to T cells to activate them and start the adaptive immune response [11,12]. These substances are transported inside the nodes (which are scattered throughout the lymphatic system) by the interstitial fluid, called *lymph* once inside the lymphatic system [12]. The main features of the lymph node from a mechanical point of view are the presence of a thin channel near the wall (*subcapsular sinus*, SCS) where the fluid can flow freely surrounding a porous core (*lymphoid compartment*, LC) that is the *parenchyma* of the lymph node [13], where the fluid can enter from the SCS through a conduit system network [14–16] formed by fibroblastic reticular cells (FRC). We can see a reconstruction of this conduit system in Figure 1. The lymph flow inside lymph nodes has various important functions, such as directing the distribution of macromolecules, enhancing ligand expression, aligning the extracellular matrix, and facilitating cell migration [11]. Additionally, the fluid flow through the endothelial monolayers and fibroblastic reticular cell (FRC) network enhances the expression of chemokines, that generate a chemokine gradient by entering the lymph node, which helps

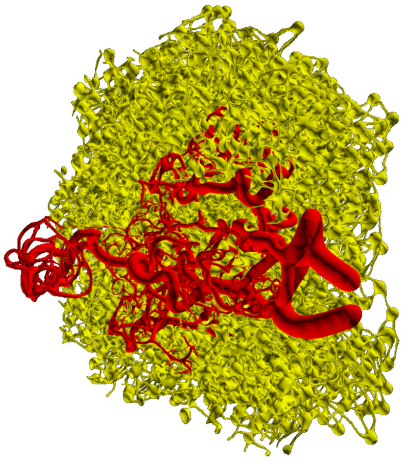

Figure 1. Reconstruction of the conduit system network (in yellow) and of the blood vessel network (in red) inside the lymphoid compartment. This figure is taken from [15] and reproduced with permission from Bocharov.

in directing the localization and migration of immune cells [11,12]. Increased fluid flow also enhances the proliferation and drug sensitivity of certain types of lymphomas [17]. The study of fluid flow is significant in understanding tumor metastasis [18] and drug transport [19]. Furthermore, damage to or removal of lymph nodes can lead to lymphœdema [20,21], a condition related to inadequate lymph transport [20].In particular, in this paper we focus our attention on the porous region of the lymph node (the LC) and the fluid exchange between the node and the blood vessels, which are only in this part of the node [22–24]; using the hypothesis of axisymmetry and isotropy of the porous medium, we find an explicit solution and analyze it by varying physiological parameters related to the lymph node.

As far as we know, the lymph flow through a lymph node has not been extensively explored from a mechanical and fluid dynamical perspective, and only a few models in the literature try to describe the behavior of a lymph node (LN) from a fluid dynamical point of view [25,26]. In [27,28] they simulate the fluid flow inside the lymph node using an image-based modeling approach to investigate how the internal structure of the node affects the fluid flow pathways within the node. In [22] they developed a computational flow model based on the mouse popliteal LN, and they identify the important system characteristics by doing a parameter sensitivity analysis. In [15] they propose an object-oriented computational algorithm to model the 3D geometry of the fibroblastic reticular cell graph network and the microvasculature, and then they analyze the lymph flow properties through the edges and the vertex of the conduit network. In [16] they developed a computational modeling algorithm that generates the conduit system graph network and then they study the fluid flow inside them imposing momentum balance along each segment and mass conservation in every node of the network. In [29] they developed a microfluidic platform replicating the lymph node microenvironment, they simulate the fluid flow in this microenvironment and then they visualize the direction of the fluid flow within the device using live imaging microscopy. Another microfluidic platform was developed by [18] that recreates the fluid dynamics of the lymph node's subcapsular sinus microenvironment; they estimate the levels of wall shear stress and evaluate how physiological flow patterns impact the adhesion of metastatic cancer cells. Ref. [30] developed an artificial neural network model to describe the lymph node drainage function. The first attempts to describe the fluid flow in the lymph node from a more explicit point of view are in [31,32], where an explicit and a numerical solution are presented in a time-dependent setting in simplified geometries (a very idealized geometry for [31] and a spherical geometry in [32]), without considering the drainage of the blood vessels. The model presented in this work allows us to describe the blood vessel's drainage

function in the lymph node considering the multiscale nature of the latter, obtaining a rigorous mathematical model using the asymptotic homogenization technique that describes the fluid flow inside both the FRC and the blood vessels networks. Moreover, thanks to the fact that we start with a formulation that is already smoothed out, we do not need precise information about the microstructure geometry of the lymph node, which is in general very complex and hard to describe.

The work is organized as follows. In Section 1, we define the starting equations of our problem. We formulate the balance equations of Continuum Mechanics and the corresponding boundary conditions. In Section 2 we use the asymptotic homogenization technique to find the equations that describe the motion of the fluid at the macroscale, one starting with the Darcy-Brinkman equation and the other with the Darcy equation, and to describe the fluid exchange between them. In Section 3, we find the macroscopic equations by averaging the leading order terms of the asymptotic expansion. In Section 4 we analyze the difference in having as a microscale cell problem Darcy, Darcy-Brinkman, or Stokes, finding an explicit result to the microscale cell problem in a specific case. In Section 5, we find the macroscopic explicit solution in a sphere with axisymmetry and isotropic permeability in terms of Bessel's and Legendre's polynomials. Finally, in Section 6 we analyze the solution found in Section 5 with lymph node physiological data obtained from the literature.

1. Statement of the problem

Let us consider a domain $\Omega = \Omega_v \cup \Omega_m$, where Ω_m and Ω_v are the portions of the domain that indicate two different phases. The labels m and v stand for the *matrix* and the *vessel* regions, respectively.

We use Darcy equation with inhomogeneous body forces to describe the fluid flow in the domain Ω_v [10]:

$$\begin{cases} \boldsymbol{u}_v(\boldsymbol{x}) = -\hat{\boldsymbol{K}}_v(\boldsymbol{x})\left(\nabla p_v(\boldsymbol{x}) - \boldsymbol{f}_v(\boldsymbol{x})\right) & \text{in } \Omega_v \\ \nabla \cdot \boldsymbol{u}_v(\boldsymbol{x}) = 0 & \text{in } \Omega_v. \end{cases} \tag{1.1}$$

The Darcy-Brinkman equation with inhomogeneous body forces in the phase Ω_m can be written as:

$$\begin{cases} -\nabla p_m(\boldsymbol{x}) - \hat{\boldsymbol{K}}_m^{-1}(\boldsymbol{x})\boldsymbol{u}_m(\boldsymbol{x}) + \mu_e \Delta \boldsymbol{u}_m(\boldsymbol{x}) + \boldsymbol{f}_m(\boldsymbol{x}) = \boldsymbol{0} & \text{in } \Omega_m \\ \nabla \cdot \boldsymbol{u}_m(\boldsymbol{x}) = 0 & \text{in } \Omega_m. \end{cases} \tag{1.2}$$

Here we are considering two fluid phases: one in Ω_v and one in Ω_m. For $\gamma = v, m$, $\boldsymbol{u}_\gamma$ is the velocity of the fluid, p_γ the pressure, $\boldsymbol{f}_\gamma$ the external force density, $\hat{\boldsymbol{K}}_\gamma(\boldsymbol{x})$ is *hydraulic conductivity tensor*, which is given by the permeability tensor divided by the viscosity μ of the fluid, and μ_e is the *effective viscosity*. We assume that the hydraulic conductivity tensor is symmetric and positive definite, that is

$$\hat{\boldsymbol{K}}_\gamma(\boldsymbol{x}) = \hat{\boldsymbol{K}}_\gamma^T(\boldsymbol{x}), \quad \forall \boldsymbol{a} \neq \boldsymbol{0} : \boldsymbol{a} \cdot \hat{\boldsymbol{K}}_\gamma(\boldsymbol{x}) \cdot \boldsymbol{a} > 0.$$

As our starting points are the Darcy and Darcy-Brinkman representations, the pore structure is considered already smoothed out, and the microscale geometry information is encoded in the hydraulic conductivity $\hat{\boldsymbol{K}}_\gamma(\boldsymbol{x})$.

The interface conditions are prescribed as follows:

$$\begin{cases} \boldsymbol{u}_v(\boldsymbol{x}) \cdot \boldsymbol{n} = \boldsymbol{u}_m(\boldsymbol{x}) \cdot \boldsymbol{n} = L_p(p_m(\boldsymbol{x}) - p_v(\boldsymbol{x}) - \bar{p}) & \text{on } \Gamma \\ \boldsymbol{u}_m(\boldsymbol{x}) \cdot \boldsymbol{\tau} = -\dfrac{\sqrt{\mu \hat{\boldsymbol{K}}_m(\boldsymbol{x})}}{\alpha}\left[(\boldsymbol{n} \cdot \nabla)\, \boldsymbol{u}_m(\boldsymbol{x})\right] \cdot \boldsymbol{\tau} & \text{on } \Gamma, \end{cases} \tag{1.3}$$

where $\Gamma = \partial\Omega_m \cap \partial\Omega_v$ is the interface between the domains Ω_v and Ω_m, $\boldsymbol{n}$ the outer normal to Ω_m, $\boldsymbol{\tau}$ any tangential vector to Γ, $\bar{p}$ is a constant and α is a constant that must be found with experiments. The second equation of (1.3) is the *Beavers-Joseph-Saffman boundary condition*

[33], which is a quite general interface condition on the tangent component of the velocity; instead, for the normal component of the velocity, we impose the interface condition described by the first equation of (1.3). We impose this type of interface condition having in mind biological applications of this model (such as lymph nodes, tumors, etc...); indeed, if we have $\bar{p} = \sigma(\pi_m - \pi_v)$, we obtain the *Starling equation* [34,35], which describes the fluid exchange between two different phases separated by a membrane, where σ is the *Staverman's reflection coefficient*, π_v the *oncotic pressure of phase* Ω_v and π_m the *oncotic pressure of phase* Ω_m. For simplicity, in this work, we assume that the oncotic pressures π_v and π_m are constant, although in general, they can depend on the concentration of solutes which vary over time and space [36,37]. The quantity L_p is given by experimental measurements and depends on both the geometry and the tissue wall material of the intersection Γ. Nevertheless, our model remains valid for other choices of boundary conditions.

Now we want to write the Darcy-Brinkman equation and the interface conditions in a non-dimensional form; we define the following non-dimensional quantities (denoted with a prime symbol):

$$p = Pp', \quad \boldsymbol{u} = U\boldsymbol{u}', \quad \boldsymbol{x} = L\boldsymbol{x}', \quad \epsilon = \frac{d}{L},$$

where P is the *characteristic pressure*, U is the *characteristic velocity*, d is the *fine scale length* and L is the *coarse scale length*. In particular, d physically represents the distance between two vascularised regions. Here we are not resolving the fine details characterising individual vessels and we instead represent the vascular network region as a domain Ω_v geometrically consisting of interconnected cylinders (see Figure 2), where Darcy's law holds. As such, d is then identified as the distance between two such adjacent cylinders. C is a *representative pressure gradient* (with $P = CL$), say:

$$C = \frac{U}{K_{\text{ref}}},$$

where K_{ref} is the representative (scalar) value for the hydraulic conductivity given by

$$K_{\text{ref}} \approx \frac{d^2}{\mu},$$

and we set

$$\boldsymbol{K}' = \frac{\hat{\boldsymbol{K}}}{K_{\text{ref}}}, \qquad \boldsymbol{f}_m' = \frac{\boldsymbol{f}_m}{C}.$$

Substituting into (1.2) and omitting the primes, we obtain:

$$\begin{cases} -\nabla p_m(\boldsymbol{x}) - \boldsymbol{K}_m^{-1}(\boldsymbol{x})\boldsymbol{u}_m(\boldsymbol{x}) + \hat{\mu}\Delta\boldsymbol{u}_m(\boldsymbol{x}) + \boldsymbol{f}_m(\boldsymbol{x}) = \boldsymbol{0} & \text{in } \Omega_m, \\ \nabla \cdot \boldsymbol{u}_m(\boldsymbol{x}) = 0 & \text{in } \Omega_m, \end{cases} \tag{1.4}$$

where

$$\hat{\mu} = \frac{K_{\text{ref}}\,\mu_e}{L^2}.$$

Assuming that $\mu_e \approx \mu$, we have $\hat{\mu} \approx O(\epsilon^2)$.

Substituting these relations into (1.1) and (1.4), we obtain the non-dimensional equations:

$$\begin{cases} \boldsymbol{u}_v(\boldsymbol{x}) = -\boldsymbol{K}_v(\boldsymbol{x})\left(\nabla p_v(\boldsymbol{x}) - \boldsymbol{f}_v(\boldsymbol{x})\right) & \text{in } \Omega_v \\ \nabla \cdot \boldsymbol{u}_v(\boldsymbol{x}) = 0 & \text{in } \Omega_v, \end{cases} \tag{1.5}$$

$$\begin{cases} -\nabla p_m(\boldsymbol{x}) - \boldsymbol{K}_m^{-1}(\boldsymbol{x})\boldsymbol{u}_m(\boldsymbol{x}) + \epsilon^2\mu^*\Delta\boldsymbol{u}_m(\boldsymbol{x}) + \boldsymbol{f}_m(\boldsymbol{x}) = \boldsymbol{0} & \text{in } \Omega_m, \\ \nabla \cdot \boldsymbol{u}_m(\boldsymbol{x}) = 0 & \text{in } \Omega_m, \end{cases} \tag{1.6}$$

where $\mu^* = \dfrac{\mu_e}{\mu}$.

Now we want to non-dimensionalize the interface conditions (1.3): by the Starling equation, the flux J_v passing through the interface between the two phases is given by

$$J_v = L_p \bar{S} \left(p_m(\boldsymbol{x}, t) - p_v(\boldsymbol{x}, t) - \bar{p} \right),$$

where $\bar{S}$ is the total exchange surface density. From the fact that d is related to the distance between the vessels of the domain Ω_v, we have

$$\bar{S} \propto \frac{L}{d} = \frac{1}{\epsilon}.$$

It is likely that the measured flux of a specific area of tissue will remain finite, even if the number of capillaries and their total surface area within that volume increases; hence we need to scale the interface condition by ϵ to have a finite flux. The same conclusion can also be recovered for the Beavers-Joseph-Saffman interface condition (see [36] for more details).

Then, if we non-dimensionalize and we substitute the previous fact into equation (1.3) we have:

$$\begin{cases} \boldsymbol{u}_v(\boldsymbol{x}) \cdot \boldsymbol{n} = \boldsymbol{u}_m(\boldsymbol{x}) \cdot \boldsymbol{n} = \epsilon \bar{L}_p (p_m(\boldsymbol{x}) - p_v(\boldsymbol{x}) - \bar{p}) & \text{on } \Gamma \\ \boldsymbol{u}_m(\boldsymbol{x}) \cdot \boldsymbol{\tau} = -\epsilon \dfrac{\sqrt{\boldsymbol{K}_m(\boldsymbol{x})}}{\alpha} \left[(\boldsymbol{n} \cdot \nabla) \, \boldsymbol{u}_m(\boldsymbol{x}) \right] \cdot \boldsymbol{\tau} & \text{on } \Gamma, \end{cases} \tag{1.7}$$

where $\bar{L}_p = \frac{L_p \mu L^2}{d^3}$ [36].

2. Asymptotic homogenization

In this section, we employ the asymptotic homogenization technique [3,4] to derive a continuum macroscale model for the systems (1.5)–(1.7). Since we suppose $\epsilon = \frac{d}{L} \ll 1$, we enforce the sharp length scale separation between d (fine scale) and L (coarse scale) and we decouple spatial scales by introducing a new local variable

$$\boldsymbol{y} = \frac{\boldsymbol{x}}{\epsilon}, \tag{2.1}$$

where $\boldsymbol{x}$ and $\boldsymbol{y}$ represent the coarse and fine scale spatial coordinates, respectively. They have to be formally considered independent variables. From now on, p_γ, $\boldsymbol{u}_\gamma$, $\boldsymbol{K}_\gamma$, and $\boldsymbol{f}_\gamma$ (where $\gamma = m, v$) are assumed to depend on both $\boldsymbol{x}$ and $\boldsymbol{y}$.

Before we start with the asymptotic homogenization technique, we recall some assumptions concerning the geometry of the multiscale problem:

- *Local periodicity*: we assume that p_γ, $\boldsymbol{u}_\gamma$, $\boldsymbol{K}_\gamma$, and $\boldsymbol{f}_\gamma$ are $\boldsymbol{y}$-periodic. This assumption allows us to study fine scale variations of the fields on a restricted portion of the domain. In particular, we have that Ω is the periodic cell domain, and Ω_m and Ω_v are the portions of the domain Ω related to the two different phases.
- *Macroscopic uniformity*: we neglect geometric variations of the cell and inclusions with respect to the coarse scale variable $\boldsymbol{x}$. Thanks to this assumption, we can consider only one periodic cell Ω_γ for every macroscale point $\boldsymbol{x}$, and we have that

$$\nabla_{\boldsymbol{x}} \cdot \int_{\Omega_\gamma} (\cdot) d\boldsymbol{y} = \int_{\Omega_\gamma} \nabla_{\boldsymbol{x}} \cdot (\cdot) d\boldsymbol{y}. \tag{2.2}$$

The differential operator transforms accordingly

$$\nabla \to \nabla_{\boldsymbol{x}} + \frac{1}{\epsilon} \nabla_{\boldsymbol{y}}. \tag{2.3}$$

Now we employ a power series representation with respect to ϵ as follows (with $\gamma = m, v$):

$$\boldsymbol{u}_\gamma(\boldsymbol{x}, \boldsymbol{y}) \equiv \boldsymbol{u}_\gamma^\epsilon(\boldsymbol{x}, \boldsymbol{y}) = \sum_{l=0}^{\infty} \boldsymbol{u}_\gamma^{(l)}(\boldsymbol{x}, \boldsymbol{y}) \epsilon^l, \tag{2.4}$$

$$p_\gamma(\boldsymbol{x},\boldsymbol{y}) \equiv p_\gamma^\epsilon(\boldsymbol{x},\boldsymbol{y}) = \sum_{l=0}^{\infty} p_\gamma^{(l)}(\boldsymbol{x},\boldsymbol{y})\epsilon^l, \tag{2.5}$$

$$\boldsymbol{f}_\gamma(\boldsymbol{x},\boldsymbol{y}) \equiv \boldsymbol{f}_\gamma^\epsilon(\boldsymbol{x},\boldsymbol{y}) = \sum_{l=0}^{\infty} \boldsymbol{f}_\gamma^{(l)}(\boldsymbol{x},\boldsymbol{y})\epsilon^l. \tag{2.6}$$

Substituting the power series representations (2.4), (2.5), (2.6) and the differential operator (2.3) into the non-dimensionalized Darcy equation (1.5), the Darcy-Brinkman equation (1.6) and the interface conditions (1.7), we have:

$$\begin{cases} \epsilon \boldsymbol{u}_v^\epsilon(\boldsymbol{x},\boldsymbol{y}) + \epsilon \boldsymbol{K}_v(\boldsymbol{x},\boldsymbol{y})\nabla_{\boldsymbol{x}} p_v^\epsilon(\boldsymbol{x},\boldsymbol{y}) + \boldsymbol{K}_v(\boldsymbol{x},\boldsymbol{y})\nabla_{\boldsymbol{y}} p_v^\epsilon(\boldsymbol{x},\boldsymbol{y}) - \epsilon \boldsymbol{K}_v(\boldsymbol{x},\boldsymbol{y})\boldsymbol{f}_v^\epsilon(\boldsymbol{x},\boldsymbol{y}) = \boldsymbol{0} & \text{in } \Omega_v, \\ \epsilon \nabla_{\boldsymbol{x}} \cdot \boldsymbol{u}_v^\epsilon(\boldsymbol{x},\boldsymbol{y}) + \nabla_{\boldsymbol{y}} \cdot \boldsymbol{u}_v^\epsilon(\boldsymbol{x},\boldsymbol{y}) = 0 & \text{in } \Omega_v, \end{cases} \tag{2.7}$$

$$\begin{cases} -\epsilon \nabla_{\boldsymbol{x}} p_m^\epsilon(\boldsymbol{x},\boldsymbol{y}) - \nabla_{\boldsymbol{y}} p_m^\epsilon(\boldsymbol{x},\boldsymbol{y}) - \epsilon \boldsymbol{K}_m^{-1}(\boldsymbol{x},\boldsymbol{y})\boldsymbol{u}_m^\epsilon(\boldsymbol{x},\boldsymbol{y}) \\ +\mu^* \epsilon^3 \Delta_{\boldsymbol{x}} \boldsymbol{u}_m^\epsilon(\boldsymbol{x},\boldsymbol{y}) + \mu^* \epsilon \Delta_{\boldsymbol{y}} \boldsymbol{u}_m^\epsilon(\boldsymbol{x},\boldsymbol{y}) + \mu^* \epsilon^2 \nabla_{\boldsymbol{x}} \cdot (\nabla_{\boldsymbol{y}} \boldsymbol{u}_m^\epsilon(\boldsymbol{x},\boldsymbol{y})) \\ +\mu^* \epsilon^2 \nabla_{\boldsymbol{y}} \cdot (\nabla_{\boldsymbol{x}} \boldsymbol{u}_m^\epsilon(\boldsymbol{x},\boldsymbol{y})) + \epsilon \boldsymbol{f}_m^\epsilon(\boldsymbol{x},\boldsymbol{y}) = \boldsymbol{0}, & \text{in } \Omega_m \\ \epsilon \nabla_{\boldsymbol{x}} \cdot \boldsymbol{u}_m^\epsilon(\boldsymbol{x},\boldsymbol{y}) + \nabla_{\boldsymbol{y}} \cdot \boldsymbol{u}_m^\epsilon(\boldsymbol{x},\boldsymbol{y}) = 0 & \text{in } \Omega_m, \end{cases} \tag{2.8}$$

$$\begin{cases} \boldsymbol{u}_v^\epsilon(\boldsymbol{x},\boldsymbol{y}) \cdot \boldsymbol{n} = \boldsymbol{u}_m^\epsilon(\boldsymbol{x},\boldsymbol{y}) \cdot \boldsymbol{n} = \epsilon \bar{L}_p (p_m^\epsilon(\boldsymbol{x},\boldsymbol{y}) - p_v^\epsilon(\boldsymbol{x},\boldsymbol{y}) - \bar{p}) & \text{on } \Gamma \\ \boldsymbol{u}_m^\epsilon(\boldsymbol{x},\boldsymbol{y}) \cdot \boldsymbol{\tau} = -\epsilon \dfrac{\sqrt{\boldsymbol{K}_m(\boldsymbol{x},\boldsymbol{y})}}{\alpha} \left[\left(\boldsymbol{n} \cdot \left(\nabla_{\boldsymbol{x}} + \dfrac{1}{\epsilon} \nabla_{\boldsymbol{y}} \right) \right) \boldsymbol{u}_m^\epsilon(\boldsymbol{x},\boldsymbol{y}) \right] \cdot \boldsymbol{\tau} & \text{on } \Gamma. \end{cases} \tag{2.9}$$

If we collect the terms of order ϵ^0 in systems (2.7) and (2.8):

$$\nabla_{\boldsymbol{y}} p_v^{(0)}(\boldsymbol{x},\boldsymbol{y}) = \boldsymbol{0} \quad \Rightarrow \quad p_v^{(0)} = p_v^{(0)}(\boldsymbol{x}), \tag{2.10}$$

$$\nabla_{\boldsymbol{y}} p_m^{(0)}(\boldsymbol{x},\boldsymbol{y}) = \boldsymbol{0} \quad \Rightarrow \quad p_m^{(0)} = p_m^{(0)}(\boldsymbol{x}), \tag{2.11}$$

$$\nabla_{\boldsymbol{y}} \cdot \boldsymbol{u}_v^{(0)}(\boldsymbol{x},\boldsymbol{y}) = 0, \tag{2.12}$$

$$\nabla_{\boldsymbol{y}} \cdot \boldsymbol{u}_m^{(0)}(\boldsymbol{x},\boldsymbol{y}) = 0, \tag{2.13}$$

and for the interface conditions (2.9):

$$\boldsymbol{u}_m^{(0)}(\boldsymbol{x},\boldsymbol{y}) \cdot \boldsymbol{n} = \boldsymbol{u}_v^{(0)}(\boldsymbol{x},\boldsymbol{y}) \cdot \boldsymbol{n} = 0 \quad \text{on } \Gamma, \tag{2.14}$$

$$\boldsymbol{u}_m^{(0)}(\boldsymbol{x},\boldsymbol{y}) \cdot \boldsymbol{\tau} = -\frac{\sqrt{\boldsymbol{K}_m(\boldsymbol{x},\boldsymbol{y})}}{\alpha} \left[(\boldsymbol{n} \cdot \nabla_{\boldsymbol{y}}) \boldsymbol{u}_m^{(0)}(\boldsymbol{x},\boldsymbol{y}) \right] \cdot \boldsymbol{\tau} \quad \text{on } \Gamma. \tag{2.15}$$

Collecting the terms of order ϵ^1 in systems (2.7), (2.8) and in the interface conditions (2.9), we obtain:

$$\boldsymbol{u}_v^{(0)}(\boldsymbol{x},\boldsymbol{y}) + \boldsymbol{K}_v(\boldsymbol{x},\boldsymbol{y}) \left(\nabla_{\boldsymbol{x}} p_v^{(0)}(\boldsymbol{x}) + \nabla_{\boldsymbol{y}} p_v^{(1)}(\boldsymbol{x},\boldsymbol{y}) - \boldsymbol{f}_v^{(0)}(\boldsymbol{x},\boldsymbol{y}) \right) = \boldsymbol{0} \quad \text{in } \Omega_v, \tag{2.16}$$

$$\nabla_{\boldsymbol{x}} \cdot \boldsymbol{u}_v^{(0)}(\boldsymbol{x},\boldsymbol{y}) + \nabla_{\boldsymbol{y}} \cdot \boldsymbol{u}_v^{(1)}(\boldsymbol{x},\boldsymbol{y}) = 0 \quad \text{in } \Omega_v, \tag{2.17}$$

$$\begin{aligned} -\nabla_{\boldsymbol{x}} p_m^{(0)}(\boldsymbol{x}) - \nabla_{\boldsymbol{y}} p_m^{(1)}(\boldsymbol{x},\boldsymbol{y}) - \boldsymbol{K}_m^{-1}(\boldsymbol{x},\boldsymbol{y})\boldsymbol{u}_m^{(0)}(\boldsymbol{x},\boldsymbol{y}) + \mu^* \Delta_{\boldsymbol{y}} \boldsymbol{u}_m^{(0)}(\boldsymbol{x},\boldsymbol{y}) \\ + \boldsymbol{f}_m^{(0)}(\boldsymbol{x},\boldsymbol{y}) = \boldsymbol{0} \quad \text{in } \Omega_m, \end{aligned} \tag{2.18}$$

$$\nabla_{\boldsymbol{x}} \cdot \boldsymbol{u}_m^{(0)}(\boldsymbol{x},\boldsymbol{y}) + \nabla_{\boldsymbol{y}} \cdot \boldsymbol{u}_m^{(1)}(\boldsymbol{x},\boldsymbol{y}) = 0 \quad \text{on } \Omega_m, \tag{2.19}$$

$$\boldsymbol{u}_m^{(1)}(\boldsymbol{x},\boldsymbol{y}) \cdot \boldsymbol{n} = \boldsymbol{u}_v^{(1)}(\boldsymbol{x},\boldsymbol{y}) \cdot \boldsymbol{n} = \bar{L}_p \left(p_m^{(0)}(\boldsymbol{x}) - p_v^{(0)}(\boldsymbol{x}) - \bar{p} \right) \quad \text{on } \Gamma, \tag{2.20}$$

$$\boldsymbol{u}_m^{(1)}(\boldsymbol{x},\boldsymbol{y}) \cdot \boldsymbol{\tau} = -\frac{\sqrt{\boldsymbol{K}_m(\boldsymbol{x},\boldsymbol{y})}}{\alpha} \left[(\boldsymbol{n} \cdot \nabla_{\boldsymbol{x}}) \boldsymbol{u}_m^{(0)}(\boldsymbol{x},\boldsymbol{y}) + (\boldsymbol{n} \cdot \nabla_{\boldsymbol{y}}) \boldsymbol{u}_m^{(1)}(\boldsymbol{x},\boldsymbol{y}) \right] \cdot \boldsymbol{\tau} \quad \text{on } \Gamma. \tag{2.21}$$

Applying the $\nabla_{\boldsymbol{y}}\cdot$ operator to the equation (2.16) and using the equation (2.12), we obtain

$$\nabla_{\boldsymbol{y}}\cdot\left[\boldsymbol{K}_v(\boldsymbol{x},\boldsymbol{y})\left(\nabla_{\boldsymbol{x}}p_v^{(0)}(\boldsymbol{x})+\nabla_{\boldsymbol{y}}p_v^{(1)}(\boldsymbol{x},\boldsymbol{y})-\boldsymbol{f}_v^{(0)}(\boldsymbol{x},\boldsymbol{y})\right)\right]=0\quad\text{in }\Omega_v,\tag{2.22}$$

and the boundary condition (2.14) becomes:

$$\left[\boldsymbol{K}_v(\boldsymbol{x},\boldsymbol{y})\left(\nabla_{\boldsymbol{x}}p_v^{(0)}(\boldsymbol{x})+\nabla_{\boldsymbol{y}}p_v^{(1)}(\boldsymbol{x},\boldsymbol{y})-\boldsymbol{f}_v^{(0)}(\boldsymbol{x},\boldsymbol{y})\right)\right]\cdot\boldsymbol{n}=0\quad\text{on }\Gamma.\tag{2.23}$$

Since the problem is linear and the vector function $\nabla_{\boldsymbol{x}}p^{(0)}$ is $\boldsymbol{y}$-constant, we state the following ansatz of the solution:

$$p_v^{(1)}(\boldsymbol{x},\boldsymbol{y})=\boldsymbol{g}_v(\boldsymbol{x},\boldsymbol{y})\cdot\nabla_{\boldsymbol{x}}p_v^{(0)}(\boldsymbol{x})+\tilde{g}_v(\boldsymbol{x},\boldsymbol{y}).\tag{2.24}$$

Equation (2.24) is a solution of the problem (2.22) and (2.23) (up to a $\boldsymbol{y}$-constant function), provided that the auxiliary vector field $\boldsymbol{g}_v$ and the auxiliary scalar function $\tilde{g}_v$ solve the following cell problems:

$$\begin{cases}\nabla_{\boldsymbol{y}}\cdot\left[\nabla_{\boldsymbol{y}}\boldsymbol{g}_v(\boldsymbol{x},\boldsymbol{y})\boldsymbol{K}_v(\boldsymbol{x},\boldsymbol{y})^T\right]=-\nabla_{\boldsymbol{y}}\cdot\boldsymbol{K}_v(\boldsymbol{x},\boldsymbol{y})^T, & \text{in }\Omega_v\\ \left[\nabla_{\boldsymbol{y}}\boldsymbol{g}_v(\boldsymbol{x},\boldsymbol{y})\boldsymbol{K}_v(\boldsymbol{x},\boldsymbol{y})^T\right]\cdot\boldsymbol{n}=-\boldsymbol{K}_v(\boldsymbol{x},\boldsymbol{y})^T\cdot\boldsymbol{n} & \text{on }\Gamma,\end{cases}\tag{2.25}$$

$$\begin{cases}\nabla_{\boldsymbol{y}}\cdot\left[\boldsymbol{K}_v(\boldsymbol{x},\boldsymbol{y})\nabla_{\boldsymbol{y}}\tilde{g}_v(\boldsymbol{x},\boldsymbol{y})\right]=\nabla_{\boldsymbol{y}}\cdot\boldsymbol{K}_v(\boldsymbol{x},\boldsymbol{y})\boldsymbol{f}_v^0(\boldsymbol{x},\boldsymbol{y}), & \text{in }\Omega_v\\ \left[\boldsymbol{K}_v(\boldsymbol{x},\boldsymbol{y})\nabla_{\boldsymbol{y}}\tilde{g}_v(\boldsymbol{x},\boldsymbol{y})\right]\cdot\boldsymbol{n}=\boldsymbol{K}_v(\boldsymbol{x},\boldsymbol{y})\boldsymbol{f}_v^0(\boldsymbol{x},\boldsymbol{y})\cdot\boldsymbol{n} & \text{on }\Gamma.\end{cases}\tag{2.26}$$

Moreover, we impose that $\langle\boldsymbol{g}_v(\boldsymbol{x},\boldsymbol{y})\rangle_{\Omega_v}=0$ and $\langle\tilde{g}_v(\boldsymbol{x},\boldsymbol{y})\rangle_{\Omega_m}=0$ to ensure the uniqueness of the solution, where $\langle\cdot\rangle_{\Omega_\gamma}$ is defined as

$$\langle h\rangle_{\Omega_\gamma}=\frac{1}{|\Omega_\gamma|}\int_{\Omega_\gamma}h d\boldsymbol{y}.\tag{2.27}$$

To solve the Darcy-Brinkman problem in Ω_m, since the problem is linear and the vector function $\nabla_{\boldsymbol{x}}p^{(0)}$ is $\boldsymbol{y}$-constant, we formulate the following ansatz for the solution:

$$p_m^{(1)}(\boldsymbol{x},\boldsymbol{y})=-\boldsymbol{g}_m(\boldsymbol{x},\boldsymbol{y})\cdot\nabla_{\boldsymbol{x}}p_m^{(0)}(\boldsymbol{x})+\tilde{g}_m(\boldsymbol{x},\boldsymbol{y}),\tag{2.28}$$

$$\boldsymbol{u}_m^{(0)}(\boldsymbol{x},\boldsymbol{y})=-\boldsymbol{W}_m(\boldsymbol{x},\boldsymbol{y})\nabla_{\boldsymbol{x}}p_m^{(0)}(\boldsymbol{x})+\tilde{\boldsymbol{w}}_m(\boldsymbol{x},\boldsymbol{y}).\tag{2.29}$$

Putting together equations (2.13), (2.14), (2.15) and (2.18), we obtain an auxiliary Darcy-Brinkman system in $(\boldsymbol{u}_m^{(0)},p_m^{(1)})$. Hence, we have that (2.28) and (2.29) are solutions of the problem (2.13), (2.14), (2.15) and (2.18) provided that the auxiliary vector fields $\boldsymbol{g}_m,\boldsymbol{W}_m,\tilde{\boldsymbol{w}}_m$ and the auxiliary scalar function $\tilde{g}_m$ solve the following cell problems:

$$\begin{cases}\boldsymbol{K}_m^{-1}(\boldsymbol{x},\boldsymbol{y})\boldsymbol{W}_m(\boldsymbol{x},\boldsymbol{y})-\mu^*\Delta_{\boldsymbol{y}}\boldsymbol{W}_m(\boldsymbol{x},\boldsymbol{y})-\mathbb{I}+\left(\nabla_{\boldsymbol{y}}\boldsymbol{g}_m(\boldsymbol{x},\boldsymbol{y})\right)^T=\boldsymbol{0} & \text{in }\Omega_m,\\ \nabla_{\boldsymbol{y}}\cdot\boldsymbol{W}_m(\boldsymbol{x},\boldsymbol{y})=0 & \text{in }\Omega_m,\\ \boldsymbol{W}_m(\boldsymbol{x},\boldsymbol{y})\cdot\boldsymbol{n}=0 & \text{on }\Gamma,\\ \boldsymbol{W}_m(\boldsymbol{x},\boldsymbol{y})\boldsymbol{\tau}=-\dfrac{\sqrt{\boldsymbol{K}_m(\boldsymbol{x},\boldsymbol{y})}}{\alpha}\left[\left(\nabla_{\boldsymbol{y}}\boldsymbol{W}_m(\boldsymbol{x},\boldsymbol{y})\right)\boldsymbol{n}\right]\boldsymbol{\tau} & \text{on }\Gamma,\end{cases}\tag{2.30}$$

$$\begin{cases}-\boldsymbol{K}_m^{-1}(\boldsymbol{x},\boldsymbol{y})\tilde{\boldsymbol{w}}_m(\boldsymbol{x},\boldsymbol{y})+\mu^*\Delta_{\boldsymbol{y}}\tilde{\boldsymbol{w}}_m(\boldsymbol{x},\boldsymbol{y})-\nabla_{\boldsymbol{y}}\tilde{g}_m(\boldsymbol{x},\boldsymbol{y})+\boldsymbol{f}_m^0(\boldsymbol{x},\boldsymbol{y})=\boldsymbol{0} & \text{in }\Omega_m,\\ \nabla_{\boldsymbol{y}}\cdot\tilde{\boldsymbol{w}}_m(\boldsymbol{x},\boldsymbol{y})=0 & \text{in }\Omega_m,\\ \tilde{\boldsymbol{w}}_m(\boldsymbol{x},\boldsymbol{y})\cdot\boldsymbol{n}=0 & \text{on }\Gamma,\\ \tilde{\boldsymbol{w}}_m(\boldsymbol{x},\boldsymbol{y})\cdot\boldsymbol{\tau}=-\dfrac{\sqrt{\boldsymbol{K}_m(\boldsymbol{x},\boldsymbol{y})}}{\alpha}\left[\left(\nabla_{\boldsymbol{y}}\tilde{\boldsymbol{w}}_m(\boldsymbol{x},\boldsymbol{y})\right)\boldsymbol{n}\right]\boldsymbol{\tau} & \text{on }\Gamma.\end{cases}\tag{2.31}$$

Moreover, we impose that $\langle\boldsymbol{g}_m(\boldsymbol{x},\boldsymbol{y})\rangle_{\Omega_m}=0$ and $\langle\tilde{g}_m(\boldsymbol{x},\boldsymbol{y})\rangle_{\Omega_m}=0$ to ensure the uniqueness of the solution.

3. The macroscopic model

Applying the average operator $\langle\cdot\rangle_{\Omega_m}$ to the ansatz (2.29), we obtain:

$$\langle \boldsymbol{u}_m^{(0)}(\boldsymbol{x},\boldsymbol{y})\rangle_{\Omega_m} = -\langle \boldsymbol{W}_m(\boldsymbol{x},\boldsymbol{y})\rangle_{\Omega_m}\nabla_{\boldsymbol{x}} p_m^{(0)}(\boldsymbol{x}) + \langle \tilde{\boldsymbol{w}}_m(\boldsymbol{x},\boldsymbol{y})\rangle_{\Omega_m}, \tag{3.1}$$

where $\boldsymbol{W}_m$ and $\tilde{\boldsymbol{w}}_m$ solve (2.30) and (2.31), respectively.

We recall the equation of order ϵ^1 for the divergence (2.19):

$$\nabla_{\boldsymbol{x}}\cdot \boldsymbol{u}_m^{(0)}(\boldsymbol{x},\boldsymbol{y}) + \nabla_{\boldsymbol{y}}\cdot \boldsymbol{u}_m^{(1)}(\boldsymbol{x},\boldsymbol{y}) = 0.$$

Applying the average operator, we obtain, using the macroscopic uniformity assumption (2.2):

$$\nabla_{\boldsymbol{x}}\cdot\langle \boldsymbol{u}_m^{(0)}(\boldsymbol{x},\boldsymbol{y})\rangle_{\Omega_m} + \langle\nabla_{\boldsymbol{y}}\cdot \boldsymbol{u}_m^{(1)}(\boldsymbol{x},\boldsymbol{y})\rangle_{\Omega_m} = 0.$$

Moreover, using the divergence theorem and the interface conditions (2.20):

$$\begin{aligned}\langle\nabla_{\boldsymbol{y}}\cdot \boldsymbol{u}_m^{(1)}\rangle_{\Omega_m} &= \frac{1}{|\Omega_m|}\int_{\Omega_m}\nabla_{\boldsymbol{y}}\cdot \boldsymbol{u}_m^{(1)}(\boldsymbol{x},\boldsymbol{y})d\boldsymbol{y} = \frac{1}{|\Omega_m|}\int_{\Gamma}\boldsymbol{u}_m^{(1)}(\boldsymbol{x},\boldsymbol{y})\cdot\boldsymbol{n}dS\\ &= \frac{\bar{L}_p S}{|\Omega_m|}\left[p_m^{(0)}(\boldsymbol{x}) - p_v^{(0)}(\boldsymbol{x}) - \bar{p}\right],\end{aligned} \tag{3.2}$$

where $|\Omega_m|$ is the volume fraction of the cell phase m and S is the unit cell capillary walls surface; hence we have

$$\nabla_{\boldsymbol{x}}\cdot\langle \boldsymbol{u}_m^{(0)}(\boldsymbol{x},\boldsymbol{y})\rangle_{\Omega_m} = -\frac{\bar{L}_p S}{|\Omega_m|}\left[p_m^{(0)}(\boldsymbol{x}) - p_v^{(0)}(\boldsymbol{x}) - \bar{p}\right]. \tag{3.3}$$

For the Darcy problem, we apply the average operator to the equation (2.16) and, substituting the ansatz (2.24), we obtain:

$$\begin{aligned}\langle \boldsymbol{u}_v^{(0)}(\boldsymbol{x},\boldsymbol{y})\rangle_{\Omega_v} =& -\langle \boldsymbol{K}_v(\boldsymbol{x},\boldsymbol{y}) + \boldsymbol{K}_v(\boldsymbol{x},\boldsymbol{y})(\nabla_{\boldsymbol{y}}\boldsymbol{g}_v(\boldsymbol{x},\boldsymbol{y}))^T\rangle_{\Omega_v}\nabla_{\boldsymbol{x}} p_v^{(0)}(\boldsymbol{x})\\ &- \langle \boldsymbol{K}_v(\boldsymbol{x},\boldsymbol{y})\nabla_{\boldsymbol{y}}\tilde{g}_v(\boldsymbol{x},\boldsymbol{y})\rangle_{\Omega_v} + \langle \boldsymbol{K}_v(\boldsymbol{x},\boldsymbol{y})\boldsymbol{f}_v^{(0)}(\boldsymbol{x},\boldsymbol{y})\rangle_{\Omega_v}.\end{aligned} \tag{3.4}$$

Using the same technique, applying the average operator and the divergence theorem to equation (2.17), it follows that

$$\nabla_{\boldsymbol{x}}\cdot\langle \boldsymbol{u}_v^{(0)}(\boldsymbol{x},\boldsymbol{y})\rangle_{\Omega_v} = \frac{\bar{L}_p S}{|\Omega_v|}\left[p_m^{(0)}(\boldsymbol{x}) - p_v^{(0)}(\boldsymbol{x}) - \bar{p}\right], \tag{3.5}$$

where we considered that $\boldsymbol{n}_v = -\boldsymbol{n}$.

We can write the total macroscale velocity $\boldsymbol{u}_C$ as:

$$\begin{aligned}\boldsymbol{u}_C =& |\Omega_m|\langle \boldsymbol{u}_m^{(0)}\boldsymbol{x},\boldsymbol{y})\rangle_{\Omega_m} + |\Omega_v|\langle \boldsymbol{u}_v^{(0)}(\boldsymbol{x},\boldsymbol{y})\rangle_{\Omega_v}\\ =& -|\Omega_m|\langle \boldsymbol{W}_m(\boldsymbol{x},\boldsymbol{y})\rangle_{\Omega_m}\nabla_{\boldsymbol{x}} p_m^{(0)}(\boldsymbol{x}) + |\Omega_m|\langle\tilde{\boldsymbol{w}}_m(\boldsymbol{x},\boldsymbol{y})\rangle_{\Omega_m}\\ &- |\Omega_v|\langle \boldsymbol{K}_v(\boldsymbol{x},\boldsymbol{y}) + \boldsymbol{K}_v(\boldsymbol{x},\boldsymbol{y})(\nabla_{\boldsymbol{y}}\boldsymbol{g}_v(\boldsymbol{x},\boldsymbol{y}))^T\rangle_{\Omega_v}\nabla_{\boldsymbol{x}} p_v^{(0)}(\boldsymbol{x})\\ &- |\Omega_v|\langle \boldsymbol{K}_v(\boldsymbol{x},\boldsymbol{y})\nabla_{\boldsymbol{y}}\tilde{g}_v(\boldsymbol{x},\boldsymbol{y})\rangle_{\Omega_v} + |\Omega_v|\langle \boldsymbol{K}_v(\boldsymbol{x},\boldsymbol{y})\boldsymbol{f}_v^{(0)}(\boldsymbol{x},\boldsymbol{y})\rangle_{\Omega_v}.\end{aligned} \tag{3.6}$$

Remark 1. *We notice that the fluid is macroscopically incompressible, as the macroscale divergence of the leading order average fluid velocity* (3.6) *reduces to zero by means of* (3.5) *and* (3.3)*. The two individual phases can have non zero divergences due to the fluid exchange between compartments, as in [36,38].*

Substituting (3.1) into equation (3.3) and (3.4) into equation (3.5), respectively, we obtain

$$\nabla_{\boldsymbol{x}} \cdot \left(\langle \boldsymbol{W}_m(\boldsymbol{x},\boldsymbol{y}) \rangle_{\Omega_m} \nabla_{\boldsymbol{x}} p_m^{(0)}(\boldsymbol{x}) \right) = \nabla_{\boldsymbol{x}} \cdot \langle \tilde{\boldsymbol{w}}_m(\boldsymbol{x},\boldsymbol{y}) \rangle_{\Omega_m} + \frac{\bar{L}_p S}{|\Omega_m|} \left[p_m^{(0)}(\boldsymbol{x}) - p_v^{(0)}(\boldsymbol{x}) - \bar{p} \right], \tag{3.7}$$

$$\begin{aligned} \nabla_{\boldsymbol{x}} \cdot \left(\langle \boldsymbol{K}_v(\boldsymbol{x},\boldsymbol{y}) + \boldsymbol{K}_v(\boldsymbol{x},\boldsymbol{y}) (\nabla_{\boldsymbol{y}} \boldsymbol{g}_v(\boldsymbol{x},\boldsymbol{y}))^T \rangle_{\Omega_v} \nabla_{\boldsymbol{x}} p_v^{(0)} \right) &= - \nabla_{\boldsymbol{x}} \cdot \langle \boldsymbol{K}_v(\boldsymbol{x},\boldsymbol{y}) \nabla_{\boldsymbol{y}} \tilde{g}_v(\boldsymbol{x},\boldsymbol{y}) \rangle_{\Omega_v} \\ &\quad + \nabla_{\boldsymbol{x}} \cdot \langle \boldsymbol{K}_v(\boldsymbol{x},\boldsymbol{y}) \boldsymbol{f}_v^{(0)}(\boldsymbol{x},\boldsymbol{y}) \rangle_{\Omega_v} \\ &\quad - \frac{\bar{L}_p S}{|\Omega_m|} \left[p_m^{(0)}(\boldsymbol{x}) - p_v^{(0)}(\boldsymbol{x}) - \bar{p} \right]. \end{aligned} \tag{3.8}$$

The equations (3.7) and (3.8) are the classical Darcy's law diffusion problem with additional terms related to the multiscale forces [10] and the fluid exchange between phases. We note that if the multiscale forces $\boldsymbol{f}_m$ and $\boldsymbol{f}_v$ are zero, the unique solutions $\tilde{g}_v(\boldsymbol{x},\boldsymbol{y})$ and $\tilde{\boldsymbol{w}}_m(\boldsymbol{x},\boldsymbol{y})$ of the systems (2.26) and (2.31) are both zero. In this latter case, equations (3.7) and (3.8) reduce to the double Darcy's model with fluid exchange between phases as derived in [38] and subsequently solved and generalised in [39] and [36], respectively. However, even when ignoring the contributions related to the external volume loads, the final model that we have obtained differs from the one obtained in [38] due to the Darcy-Brinkman type cell problem which is to be solved to compute the hydraulic conductivity $\langle \boldsymbol{W}_m \rangle_{\Omega_m}$ for the matrix compartment Ω_m.

The equations (3.1), (3.3), (3.4), and (3.5) are in non-dimensional form. We have the following relations

$$|\Omega_m| = \frac{|\Omega_m^{\text{tot}}|}{|\Omega|}, \quad |\Omega_v| = \frac{|\Omega_v^{\text{tot}}|}{|\Omega|}, \quad S = \frac{S^{\text{tot}} d}{|\Omega|}, \tag{3.9}$$

where $|\Omega|$ is the total volume of the lymph node, $|\Omega_m^{\text{tot}}|$ is the total volume of the phase m, $|\Omega_v^{\text{tot}}|$ is the total volume of the phase v, and S^{tot} is the total vessel surface. Thanks to the above relations, we have that the equations (3.1), (3.3), (3.4), and (3.5) in the dimensional form are

$$\langle \boldsymbol{u}_m^{(0)}(\boldsymbol{x},\boldsymbol{y}) \rangle_{\Omega_m} = -\frac{d^2}{\mu} \langle \boldsymbol{W}_m(\boldsymbol{x},\boldsymbol{y}) \rangle_{\Omega_m} \nabla_{\boldsymbol{x}} p_m^{(0)}(\boldsymbol{x}) + \frac{C d^2}{\mu} \langle \tilde{\boldsymbol{w}}_m(\boldsymbol{x},\boldsymbol{y}) \rangle_{\Omega_m}, \tag{3.10}$$

$$\nabla_{\boldsymbol{x}} \cdot \langle \boldsymbol{u}_m^{(0)}(\boldsymbol{x},\boldsymbol{y}) \rangle_{\Omega_m} = -\frac{L_p S^{\text{tot}}}{|\Omega_m^{\text{tot}}|} \left[p_m^{(0)}(\boldsymbol{x}) - p_v^{(0)}(\boldsymbol{x}) - \bar{p} \right]. \tag{3.11}$$

$$\begin{aligned} \langle \boldsymbol{u}_v^{(0)}(\boldsymbol{x},\boldsymbol{y}) \rangle_{\Omega_v} &= -\frac{d^2}{\mu} \langle \boldsymbol{K}_v(\boldsymbol{x},\boldsymbol{y}) + \boldsymbol{K}_v(\boldsymbol{x},\boldsymbol{y}) (\nabla_{\boldsymbol{y}} \boldsymbol{g}_v(\boldsymbol{x},\boldsymbol{y}))^T \rangle_{\Omega_v} \nabla_{\boldsymbol{x}} p_v^{(0)}(\boldsymbol{x}) \\ &\quad - \frac{C d^2}{\mu} \langle \boldsymbol{K}_v(\boldsymbol{x},\boldsymbol{y}) \nabla_{\boldsymbol{y}} \tilde{g}_v(\boldsymbol{x},\boldsymbol{y}) \rangle_{\Omega_v} + \frac{C d^2}{\mu} \langle \boldsymbol{K}_v(\boldsymbol{x},\boldsymbol{y}) \boldsymbol{f}_v^{(0)}(\boldsymbol{x},\boldsymbol{y}) \rangle_{\Omega_v}. \end{aligned} \tag{3.12}$$

$$\nabla_{\boldsymbol{x}} \cdot \langle \boldsymbol{u}_v^{(0)}(\boldsymbol{x},\boldsymbol{y}) \rangle_{\Omega_v} = \frac{L_p S^{\text{tot}}}{|\Omega_v^{\text{tot}}|} \left[p_m^{(0)}(\boldsymbol{x}) - p_v^{(0)}(\boldsymbol{x}) - \bar{p} \right], \tag{3.13}$$

and then we call

$$\bar{\boldsymbol{K}}_m = \frac{d^2}{\mu} \langle \boldsymbol{W}_m(\boldsymbol{x},\boldsymbol{y}) \rangle_{\Omega_m}, \tag{3.14}$$

$$\bar{\boldsymbol{K}}_v = \frac{d^2}{\mu} \langle \boldsymbol{K}_v(\boldsymbol{x},\boldsymbol{y}) + \boldsymbol{K}_v(\boldsymbol{x},\boldsymbol{y}) (\nabla_{\boldsymbol{y}} \boldsymbol{g}_v(\boldsymbol{x},\boldsymbol{y}))^T \rangle_{\Omega_v}, \tag{3.15}$$

the dimensional hydraulic conductivity of the phase m and v, respectively.

4. A comparison between different fluid regimes

In this section, we want to study the differences in using Darcy, Stokes, or Darcy-Brinkman for the domain Ω_v in the cell problem. We can see the cell problem domain in Figure 2.

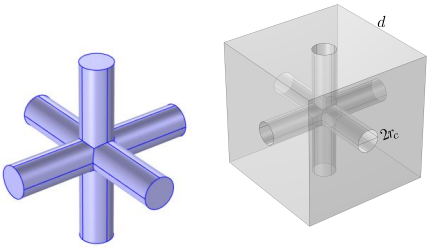

Figure 2. The cell problem domains Ω_v (blue on the left) and Ω_m (gray on the right), with the geometrical parameters in dimensional form, where r_c is the radius of the cylinders, d is the microscale variable, and $\hat{r}_c = r_c/d$.

For simplicity we focus on the case $\boldsymbol{f}_v = \boldsymbol{0}$, replacing the interface boundary conditions with the no-slip condition $\boldsymbol{u}_v = \boldsymbol{0}$ and assuming the isotropy of the porous medium, that is $\boldsymbol{K}_v = K_v\mathbb{I}$. Hence the Darcy cell problems (2.25) and (2.26) reduce to

$$\begin{cases} \nabla_{\boldsymbol{y}} \cdot [\nabla_{\boldsymbol{y}} \boldsymbol{g}_v(\boldsymbol{x},\boldsymbol{y})] = 0, & \text{in } \Omega_v \\ \nabla_{\boldsymbol{y}} \boldsymbol{g}_v(\boldsymbol{x},\boldsymbol{y}) \cdot \boldsymbol{n} = -\boldsymbol{n} & \text{on } \Gamma, \end{cases} \tag{4.1}$$

while the Darcy-Brinkman cell problems (2.30) and (2.31) reduce to

$$\begin{cases} K^{*-1}\boldsymbol{W}_v^{DB}(\boldsymbol{x},\boldsymbol{y}) - \mu^* \Delta_{\boldsymbol{y}} \boldsymbol{W}_v^{DB}(\boldsymbol{x},\boldsymbol{y}) - \mathbb{I} + \left(\nabla_{\boldsymbol{y}} \boldsymbol{g}_v^{DB}(\boldsymbol{x},\boldsymbol{y})\right)^T = \boldsymbol{0} & \text{in } \Omega_v, \\ \nabla_{\boldsymbol{y}} \cdot \boldsymbol{W}_v^{DB}(\boldsymbol{x},\boldsymbol{y}) = 0 & \text{in } \Omega_v, \\ \boldsymbol{W}_v^{DB}(\boldsymbol{x},\boldsymbol{y}) = \boldsymbol{0} & \text{on } \Gamma, \end{cases} \tag{4.2}$$

where $K^* = \dfrac{K_v\mu}{d^2}$. Finally, the cell problem for the Stokes equation is [3]

$$\begin{cases} -\Delta_{\boldsymbol{y}} \boldsymbol{W}_v^{S}(\boldsymbol{x},\boldsymbol{y}) - \mathbb{I} + \left(\nabla_{\boldsymbol{y}} \boldsymbol{g}_v^{S}(\boldsymbol{x},\boldsymbol{y})\right)^T = \boldsymbol{0} & \text{in } \Omega_v, \\ \nabla_{\boldsymbol{y}} \cdot \boldsymbol{W}_v^{S}(\boldsymbol{x},\boldsymbol{y}) = 0 & \text{in } \Omega_v, \\ \boldsymbol{W}_v^{S}(\boldsymbol{x},\boldsymbol{y}) = \boldsymbol{0} & \text{on } \Gamma. \end{cases} \tag{4.3}$$

We want to solve and compare the problems above in the cell domain Ω_v; therefore we need to compare the same quantity at the macroscale. For Darcy-Brinkman and Stokes, the dimensionalized macroscopic velocity is given by (3.10):

$$\langle \boldsymbol{u}_v^{DB/S} \rangle_{\Omega_v} = -\frac{d^2}{\mu} \langle \boldsymbol{W}_v^{DB/S} \rangle_{\Omega_v} \nabla_{\boldsymbol{x}} p^{(0)},$$

where $\boldsymbol{W}_v^{DB/S}$ takes different expressions in Darcy-Brinkman's and Stokes' cases. On the other hand, for the Darcy case we have, by equation (3.12):

$$\langle \boldsymbol{u}_v \rangle_{\Omega_v} = -K^* \frac{d^2}{\mu} \langle \mathbb{I} + (\nabla_{\boldsymbol{y}} \boldsymbol{g}_v)^T \rangle_{\Omega_v} \nabla_{\boldsymbol{x}} p^{(0)}.$$

Hence we compare $\langle \boldsymbol{W}^{DB/S} \rangle_{\Omega_v}$ for the Darcy-Brinkman and the Stokes problem and $K^* \langle \mathbb{I} + (\nabla_{\boldsymbol{y}} \boldsymbol{g}_v)^T \rangle_{\Omega_v}$ for the Darcy problem.

If we consider cylinders with a small radius, so that they have a small overlap region, we can analytically solve the previous systems up to a small error. The differential problems (4.2) and (4.3) written in terms of the auxiliary tensor $\boldsymbol{W}_v$ can be shown to correspond to three standard Darcy-Brinkman and three Stokes' systems of equations, respectively, see also [10,39]. Using the rotation invariance property of our geometry, we can choose one arbitrary row (*i.e.* direction) of $\mathbb{I}$, say $\boldsymbol{e}_3$ (the third row of $\mathbb{I}$), and we set $\boldsymbol{W}_{3,v} = \boldsymbol{W}_v \boldsymbol{e}_3$. In this case, the solution is non-zero only in the branch directed along $\boldsymbol{e}_3$, which means the only non-zero component is $\boldsymbol{W}_{3,v}\boldsymbol{e}_3 = W_{33,v}$.

Hence the solution of the system (4.3) is (see [39]):

$$W^S_{33,v} = \frac{\hat{r}_c^2 - r^2}{4}, \quad W^S_{31,v} = W^S_{32,v} = 0, \quad 0 \le r \le \hat{r}_c,$$

where $\hat{r}_c$ is the radius of the cylinder (non-dimensional). Hence we have that the resulting permeability is:

$$\langle W^S_{33,v} \rangle_{\Omega_v} = \frac{1}{|\Omega_v|} \int_0^{l_c} dz \int_0^{2\pi} d\theta \int_0^{\hat{r}_c} \frac{\hat{r}_c^2 - r^2}{4} r dr = \frac{\pi l_c \hat{r}_c^4}{8|\Omega_v|}. \tag{4.4}$$

For the system (4.2) the problem reduces to

$$W^{DB\prime\prime}_{33,v}(r) + \frac{1}{r} W^{DB\prime}_{33,v}(r) - \frac{W^{DB}_{33,v}(r)}{\mu^* K^*} = -\frac{1}{\mu^*}, \quad 0 \le r \le \hat{r}_c$$

and the solution is

$$W^{DB}_{33,v}(r) = K^* \left[1 - \frac{J_0\left(i \sqrt{\frac{1}{\mu^* K^*}} r \right)}{J_0\left(i \sqrt{\frac{1}{\mu^* K^*}} \hat{r}_c \right)} \right], \quad W^{DB}_{31,v} = W^{DB}_{32,v} = 0,$$

where J_0 is the Bessel function of the first kind of order zero. Hence we have (using the property $x^\nu J_{\nu-1} = \frac{d}{dx}\left(x^\nu J_\nu(x)\right)$):

$$\begin{aligned} \langle W^{DB}_{33,v} \rangle_{\Omega_v} &= \frac{1}{|\Omega_v|} \int_0^{l_c} dz \int_0^{2\pi} d\theta \int_0^{\hat{r}_c} K^* \left[1 - \frac{J_0\left(i \sqrt{\frac{1}{\mu^* K^*}} r \right)}{J_0\left(i \sqrt{\frac{1}{\mu^* K^*}} \hat{r}_c \right)} \right] r dr \\ &= \frac{2\pi l_c}{|\Omega_v|} K^* \left[\frac{\hat{r}_c^2}{2} + i \sqrt{\mu^* K^*} \hat{r}_c \frac{J_1\left(i \sqrt{\frac{1}{\mu^* K^*}} \hat{r}_c \right)}{J_0\left(i \sqrt{\frac{1}{\mu^* K^*}} \hat{r}_c \right)} \right]. \end{aligned} \tag{4.5}$$

To solve system (4.1), we recall that $\boldsymbol{n} = (n_1, n_2, 0) = (\cos\theta, \sin\theta, 0)$. First of all, we focus on the case $n_1 = \cos\theta$, and we call the solution $g_{v,1}$. From the periodicity condition in the $\boldsymbol{e}_3$ direction, we have that $\boldsymbol{g}_v$ does not depend on the z variable. Hence the problem reduces to

$$\frac{1}{r} \frac{\partial}{\partial r} \left(r \frac{\partial g_{v,1}}{\partial r} \right) + \frac{1}{r^2} \frac{\partial^2 g_{v,1}}{\partial \theta^2} = 0, \quad 0 \le r \le \hat{r}_c, \quad 0 \le \theta \le 2\pi.$$

Using the separation of variables $g_{v,1} = R(r)\Theta(\theta)$ and substituting into the equation above, we obtain

$$\begin{cases} r^2 R''(r) + r R'(r) - c R(r) = 0, \\ \Theta''(\theta) + c \Theta(\theta) = 0, \end{cases} \tag{4.6}$$

where c is the constant obtained by the separation of variables. From the second equation of the system (4.6), we have

$$\Theta(\theta) = A \sin(n\theta) + B \cos(n\theta), \quad n \in \mathbb{N}.$$

From the boundary condition of the system (4.1), it follows that $n = 1$. Hence the solution of the first equation of the system (4.6) is

$$R(r) = \frac{C_1}{r} + C_2 r,$$

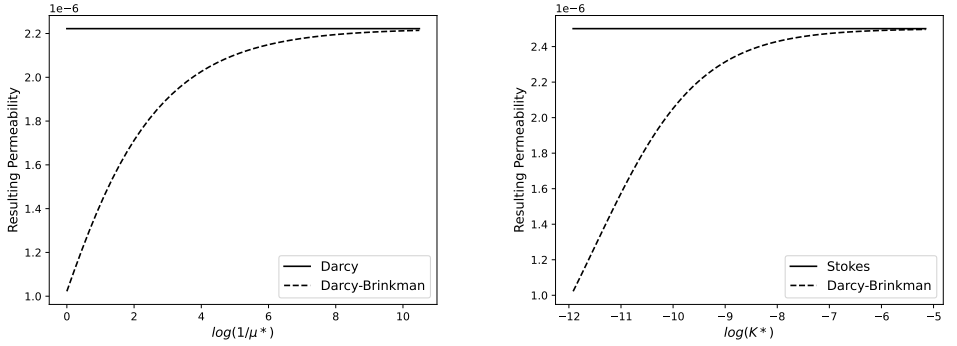

Figure 3. On the left: Darcy-Brinkman/Darcy comparison with respect to $1/\mu^*$, for $K^* = 6.67 \times 10^{-6}$. On the right: Darcy-Brinkman/Stokes comparison with respect to K^*, for $\mu^* = 1$.

μ^*	K^*	relative error
1	6.67×10^{-6}	74%
10^{-4}	6.67×10^{-6}	0.67%
10^{-6}	6.67×10^{-6}	0.067%
1	10^{-12}	0.026%

μ^*	K^*	relative error
1	6.67×10^{-6}	84%
1	10^{-4}	9.5%
1	10^{-2}	0.1%
1	1	0.001%

Table 1. Comparison between Darcy-Brinkman and Darcy (left), Darcy-Brinkman and Stokes (right).

and, from the boundary condition of (4.1) and the non-degeneracy condition in $r = 0$, we have $C_1 = 0$ and $C_2 = 1$. Hence we have

$$g_{v,1} = -r\cos\theta.$$

In the same way, for the case $n_2 = \sin\theta$ we get:

$$g_{v,2} = -r\sin\theta.$$

Hence it follows:

$$\langle(\nabla_{\boldsymbol{y}}\boldsymbol{g}_v)^T\rangle_{\Omega_v} = \frac{1}{|\Omega_v|}\int_{\Omega_v}(\nabla_{\boldsymbol{y}}\boldsymbol{g}_v)^T\,dV = -\frac{2}{3}. \tag{4.7}$$

These results are shown in Figure 3, where we set $\hat{r}_c = 7.7 \times 10^{-3}$, $|\Omega_v| = 3\pi R^2 l_c$ (the volume is indeed a bit smaller, but we are supposing that the intersection between the cylinders is negligible).

As expected, the Darcy-Brinkman equation has a Stokes/Darcy duality behavior. Indeed, suppose we decrease the relevance of the Laplace operator in the Darcy-Brinkman cell problem (4.2). In that case, we have that the solution tends to the solution of the Darcy cell problem (4.1). We can see this behavior in the left Figure 3. The resulting permeability of the cell problem (4.2) tends to the one of the cell problem (4.1). We can see this behavior even if we decrease the permeability instead of the relevance of the Laplace operator because, in this case, both the Darcy and the Darcy-Brinkman equations tend to zero. In the right Figure 3 we can see that if we increase K^* in the Darcy-Brinkman cell problem (4.2), the solution tends to that of the Stokes cell problem (4.3). Table 1 shows that, if the permeability is not too small or the Laplace operator is relevant, then the Darcy (resp. Stokes) and the Darcy-Brinkman equation give very different results; otherwise the solutions of the two problems are similar.

5. The explicit solution

In this section, we find an explicit solution to the macroscopic problem given in Section 3. More details about this section are given in Appendix A. For simplicity, we assume that the multiscale forces $\boldsymbol{f}_v^\epsilon$ and $\boldsymbol{f}_m^\epsilon$ vanish and that both porous media are isotropic, that is:

$$\bar{\boldsymbol{K}}_v = \bar{K}_v \mathbb{I}, \quad \bar{\boldsymbol{K}}_m = \bar{K}_m \mathbb{I},$$

where, from equations (3.15) and (3.14), $\bar{K}_v$ and $\bar{K}_m$ correspond to $\langle \boldsymbol{K}_v + \boldsymbol{K}_v \left(\nabla_{\boldsymbol{y}} \boldsymbol{g}_v\right)^T \rangle_{\Omega_v}$ and $\langle \frac{d^2}{\mu} \boldsymbol{W}_m \rangle_{\Omega_v}$, respectively. We have that $\bar{K}_v$ and $\bar{K}_m$ are constants due to the geometry and the hypotheses used, and they are found solving the cell problems (2.25) and (2.30), respectively, using COMSOL Multiphysics, with $\alpha = 1$ (see Appendix C for more details). We consider a spherical domain Ω, denoting by r the radial coordinate, θ the polar coordinate, and ϕ the azimuthal angle. Moreover, we assume axisymmetry with respect to the azimuthal angle ϕ. Hence our problem is:

$$\begin{cases} \Delta p_v(r,\theta) = -M_v \left[p_m(r,\theta) - p_v(r,\theta) - \bar{p}\right] & r < R,\ \theta \in [0, 2\pi[, \\ \Delta p_m(r,\theta) = M_m \left[p_m(r,\theta) - p_v(r,\theta) - \bar{p}\right] & r < R,\ \theta \in [0, 2\pi[, \\ p_v(R,\theta) = \bar{p}_v(\theta), \quad p_m(R,\theta) = \bar{p}_m(\theta) & \theta \in [0, 2\pi[, \\ \text{non-degenericity} & r = 0,\ \theta \in [0, 2\pi[, \end{cases} \tag{5.1}$$

where R is the radius of the spherical domain, $M_v = \dfrac{L_p S^{\text{tot}}}{|\Omega_v^{\text{tot}}| \bar{K}_v}$, and $M_m = \dfrac{L_p S^{\text{tot}}}{|\Omega_m^{\text{tot}}| \bar{K}_m}$.

We define the quantity

$$\psi(r,\theta) = p_m(r,\theta) - p_v(r,\theta), \tag{5.2}$$

and, taking the difference between the second and the first equation of the system (5.1), we obtain the new problem

$$\begin{cases} \Delta \psi(r,\theta) = M \left[\psi(r,\theta) - \bar{p}\right] & r < R,\ \theta \in [0, 2\pi[, \\ \psi(R,\theta) = \bar{p}_m(\theta) - \bar{p}_v(\theta), & \theta \in [0, 2\pi[, \\ \text{non-degenericity} & r = 0,\ \theta \in [0, 2\pi[, \end{cases} \tag{5.3}$$

where $M = M_v + M_m$. Defining

$$\hat{\psi}(r,\theta) = \psi(r,\theta) - \bar{p}, \tag{5.4}$$

we can reformulate the first equation of the system (5.3) as

$$\Delta \hat{\psi}(r,\theta) = M \hat{\psi}(r,\theta). \tag{5.5}$$

Details about the computations can be found in Appendix A. The solution to the problem (5.5) is the following

$$\hat{\psi}(r,\zeta) = \sum_{n=0}^{\infty} \tilde{A}_n \frac{1}{\sqrt{r}} I_{n+\frac{1}{2}} \left(\sqrt{M} r\right) P_n(\zeta), \tag{5.6}$$

where $\zeta = \cos\theta$, $I_{n+\frac{1}{2}}$ is the *modified Bessel polynomial of the first kind*, $P_n(\zeta)$ is the *Legendre polynomial of the first kind* [40], and with the boundary condition from the second equation in the system (5.3)

$$\psi(R,\zeta) = \bar{p}_m(\zeta) - \bar{p}_v(\zeta) = \sum_{n=0}^{\infty} b^{(n)} P_n(\zeta). \tag{5.7}$$

We have that $\tilde{A}_n$ is given by the boundary conditions (5.7) and it is

$$\tilde{A}_0 = \frac{\left[b^{(0)} - \bar{p}\right] \sqrt{R}}{I_{\frac{1}{2}} \left(\sqrt{M} R\right)} \quad \text{for } n = 0, \qquad \tilde{A}_n = \frac{b^{(n)} \sqrt{R}}{I_{n+\frac{1}{2}} \left(\sqrt{M} R\right)} \quad \text{for } n \in \mathbb{N}, n \neq 0. \tag{5.8}$$

The solutions of the system (5.1) are

$$p_m(r,\zeta)=\sum_{n=0}^{\infty}\left[c_1^{(n)}r^n+\frac{M_m\tilde{A}_n}{M}\frac{1}{\sqrt{r}}I_{n+\frac{1}{2}}\left(\sqrt{M}r\right)\right]P_n(\zeta), \tag{5.9}$$

$$p_v(r,\zeta)=\sum_{n=0}^{\infty}\left[d_1^{(n)}r^n-\frac{M_v\tilde{A}_n}{M}\frac{1}{\sqrt{r}}I_{n+\frac{1}{2}}\left(\sqrt{M}r\right)\right]P_n(\zeta), \tag{5.10}$$

where the constants $c_1^{(n)}$ and $d_1^{(n)}$ are found explicitly in Appendix A.

6. Application to the lymph node

In this section, we show the results given by the explicit solution with physiological data obtained or estimated by an idealized spherical mouse popliteal lymph node [32]. The lymph node is basically formed by two parts: a porous bulk region called lymphoid compartment (LC) and a thin layer against the wall where the fluid can flow freely, called subcapsular sinus (SCS) [11,41]. Due to the fact that the whole blood vasculature in the lymph node is in the LC [22–24], in this section, we apply the explicit solution found in the previous section to the LC, implemented in Matlab.

Here we have that Ω_v is the *blood vessels phase*, and Ω_m is the *interstitial phase*. The fluid exchange between these two phases is described by the Starling equation, which corresponds to choose $\bar{p}=\sigma(\pi_m-\pi_v)$. The physiological data used in this work are explained in Appendix B and are summarized in Table 2.

To find the hydraulic conductivity $\bar{K}_v$ and $\bar{K}_m$ of the dimensional macroscale equations (3.12) and (3.10) defined in (3.15) and (3.14), we solve the cell problems (2.25) and (2.30) with the body forces $\boldsymbol{f}_m=\boldsymbol{f}_v=\mathbf{0}$, $\alpha=1$, and using the microstructure parameters described in Table 2, using COMSOL Multiphysics (see Appendix C for more information about the numerical simulations). In [22] they used an interstitial hydraulic conductivity similar to those measured in LS174T tumors of the value of $\approx 2\times10^{-10}\,\frac{\mathrm{mm^3 s}}{\mathrm{mg}}$. In [27] they found an average permeability of $\approx 3.8\times10^{-5}\,\mathrm{mm}^2$ fitting the results found in their model to the data of a canine popliteal lymph node from [42]. In our model, we obtained the hydraulic conductivity $\bar{K}_m=3.65\times10^{-9}\,\frac{\mathrm{mm^3 s}}{\mathrm{mg}}$, starting with a permeability of $3.84\times10^{-9}\,\mathrm{mm}^2$ for the Darcy-Brinkman equation, taken from [16,29]. The strength of our model is to obtain a permeability for the macroscale using a rigorous homogenization method (*i.e.* asymptotic homogenization), taking into account the geometry and the differential equations used in the microscale. Moreover, we found the hydraulic conductivity and the fluid flow inside the blood vessels too in order to better describe the fluid exchange between the blood vessels and the lymph.

As boundary conditions we choose:

$$p_v(R,\zeta)=\bar{p}_v,\qquad p_m(R,\zeta)=\bar{p}_m(\zeta),$$

where $\bar{p}_v$ is a constant value given by the literature (mean blood vessels pressure), and $\bar{p}_m(\zeta)$ can be any function sufficiently regular of ζ.

To begin with (and for simplicity), we assume that $\bar{p}_m(\zeta)=\bar{p}_m$ is a fixed constant value. In this case, we can see the direction of the fluid exchange between the interstitial space and the blood vessels explicitly. Indeed, in this case, remains only the $n=0$ term (from equations (5.7), the computations in Appendix A, and from the fact that $P_0(x)=1$ we have $b^{(0)}=b_m^{(0)}-b_n^{(0)}=\bar{p}_m-\bar{p}_v$), and this implies that equation (5.6) reduces to

$$\hat{\psi}(r)=\tilde{A}_0\frac{I_{1/2}\left(\sqrt{M}r\right)}{\sqrt{r}}=\frac{\sqrt{R}I_{1/2}\left(\sqrt{M}r\right)}{\sqrt{r}I_{1/2}\left(\sqrt{M}R\right)}\left[\bar{p}_m-\bar{p}_v-\sigma(\pi_m-\pi_v)\right].$$

Name	Physiological Range/Value	Description
R	$0.49\,\text{mm}$	Macroscopic radius [18,32].
μ	$1\,\frac{\text{mg}}{\text{mm s}}$	Viscosity [20,43].
ϕ	0.75	Porosity [29].
μ_e	$\frac{\mu}{\phi}$	Effective viscosity [5,44–46].
ρ_0	$1\,\frac{\text{mg}}{\text{mm}^3}$	Density [20,43].
$\hat{K}_m$	$3.84\times10^{-9}\,\text{mm}^2$	Permeability of the interstitium [16,29].
σ	$0.88-0.9$	Staverman's coefficient [22,27,28,30].
$\pi_v-\pi_m$	$3.41\times10^{5}-2.08\times10^{6}\,\text{mPa}$	Oncotic pressure difference [22,27,28,30, 42,47–49].
L_p	$5.475\times10^{-12}-3.67\times10^{-8}\,\frac{\text{mm}}{\text{s mPa}}$	Hydraulic conductivity of the blood vessel walls [22,27,28,30].
$\bar{p}_v$	$6.67\times10^{5}-1.066\times10^{6}\,\text{mPa}$	Mean blood vessel pressure [22,27,28,30].
S^{tot}	$13.4\,\text{mm}^2$	Blood vessel surface [23,24].
$\lvert\Omega_v^{\text{tot}}\rvert$	$0.0322\,\text{mm}^3$	Blood vessel volume [23].
N	1310	Number of cells (Appendix B).
r_c	$1.7\times10^{-3}\,\text{mm}$	Microscale cylinders radius (Appendix B).
d	$2\times10^{-2}\,\text{mm}$	Microscale cylinders mean distance (Appendix B).
L	$1\,\text{mm}$	Coarse scale characteristic length.
c_0	5.6	Kozeny constant [39].
K_v	$\frac{1}{c_0\left(\frac{S^{\text{tot}}}{\lvert\Omega_v^{\text{tot}}\rvert}\right)^2}$	Hydraulic conductivity of the blood vessels using the Kozeny-Carman formula [50,51].
$\boldsymbol{f}_m$, $\boldsymbol{f}_v$	0	Body forces.
$\bar{K}_m$	$3.65\times10^{-9}\,\frac{\text{mm}^3\text{s}}{\text{mg}}$	Macroscopic interstitial hydraulic conductivity (solving system (2.30)).
$\bar{K}_v$	$4.12\times10^{-7}\,\frac{\text{mm}^3\text{s}}{\text{mg}}$	Macroscopic blood hydraulic conductivity (solving system (2.25)).

Table 2. Physiological and estimated parameters.

From the fact that (3.5) can be written as $\nabla_{\boldsymbol{x}}\cdot\langle\boldsymbol{u}_v^{(0)}(\boldsymbol{x},\boldsymbol{y})\rangle_{\Omega_v}=\dfrac{L_pS^{\text{tot}}}{|\Omega_v^{\text{tot}}|}\hat{\psi}(r)$ and recalling that $I_{1/2}(x)=\dfrac{\sqrt{\frac{2}{\pi}}\sinh(x)}{\sqrt{x}}$ is positive for every $x>0$, we have that the divergence in (3.5) has the same sign as

$$\bar{p}_m-\bar{p}_v-\sigma\left(\pi_m-\pi_v\right), \tag{6.1}$$

which is the opposite sign of the divergence in (3.3); this gives us information about the direction of the fluid exchange.

The work [52] measured that the average pressure in a lymph node is about $6.86\pm0.56\,\text{cmH}_2\text{O}\approx6.7\times10^5\pm5.5\times10^4\,\text{mPa}$, so, for now, we fix $\bar{p}_m=6.7\times10^5\,\text{mPa}$. With this value, $\sigma=0.88$ and $\Delta\pi=1.02\times10^6\,\text{mPa}$, we have that the sign of (6.1) is negative for $\bar{p}_v\lessapprox1.5676\times10^6\,\text{mPa}\approx11.8\,\text{mmHg}$ (which means that the fluid goes from the interstitial space to the blood phase), and start to have an inversion of the flow at $\bar{p}_v\approx1.5676\times10^6\,\text{mPa}\approx11.8\,\text{mmHg}$.

In Figure 4 we can see the resulting pressures p_m and p_v varying with respect to the Kozeny constant c_0. Increasing c_0 means increasing the tortuosity of the blood vessels [39], and this is

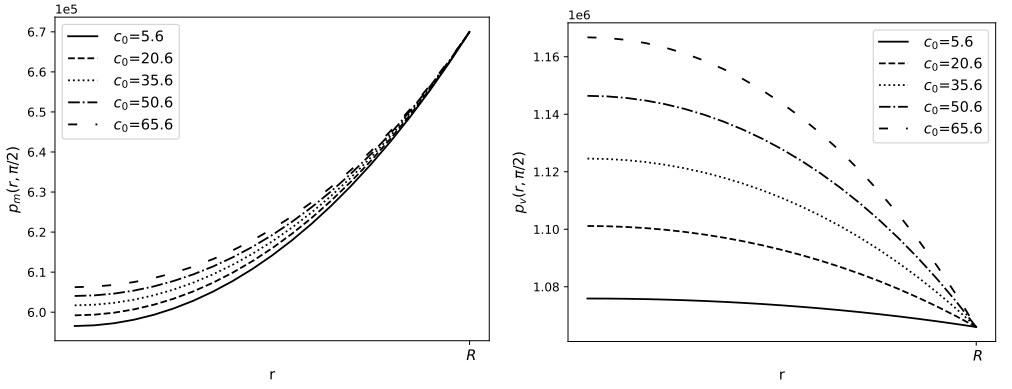

Figure 4. The variation of p_m and p_v in mPa at $\theta = \pi/2$, for some values of the Kozeny constant c_0, with $\pi_v - \pi_m = 1.02 \times 10^6$ mPa, $\bar{p}_v = 1.066 \times 10^6$ mPa, $L_p = 5.475 \times 10^{-10}$ $\frac{\text{mm}}{\text{s mPa}}$, $\bar{p}_m = 6.7 \times 10^5$ mPa and the parameters in Table 2.

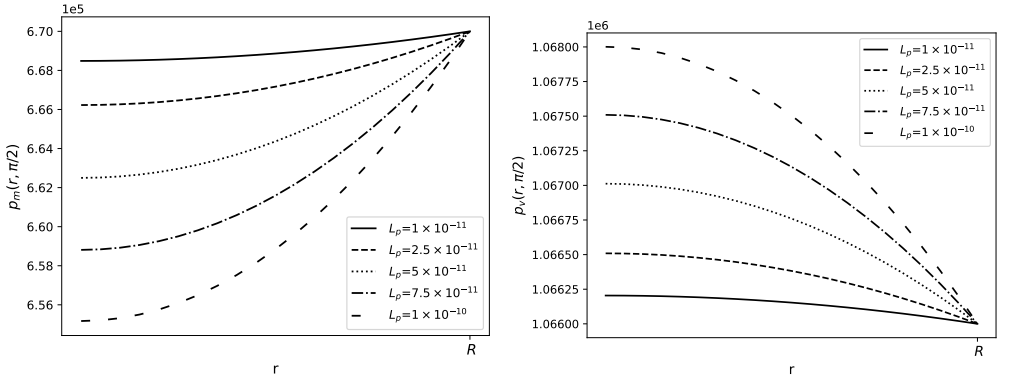

Figure 5. The variation of p_m and p_v in mPa at $\theta = \pi/2$, for some values of the hydraulic conductivity L_p in $\frac{\text{mm}}{\text{s mPa}}$, with $\pi_v - \pi_m = 1.02 \times 10^6$ mPa, $\bar{p}_v = 1.066 \times 10^6$ mPa, $\bar{p}_m = 6.7 \times 10^5$ mPa and the parameters in Table 2.

related to an increase of p_v and p_m at the center of the node, and that means that there is lesser flow from the interstitial space to the blood vessels (remembering that Darcy's law linearly relates the fluid discharge to the pressure difference, so the lymph moves accordingly to the pressure, see Figure 12 and below for more details). This is related to the fact that increasing c_0 in the Kozeny-Carman formula (see Table 2 and Appendix B) means a decrease in K_v. Consequently, an increase of the pressure p_v at the center of the node means an increase of p_m; we can see this behavior better in Figure 6. This is a parametric study with the variation of c_0 related to the tortuosity effect [39]; however, to study the role of the tortuosity in more detail, we need to take it into account in the geometry of the microscale problem, which we did not do in this case.

In Figure 5 we can see the resulting pressures p_m and p_v varying with respect to the hydraulic conductivity of the blood vessel walls L_p. Increasing L_p means a decrease of p_m and an increase of p_v at the center of the node, meaning a higher flow from the interstitial space to the blood vessels (as expected).

In Figure 7 we can see the resulting pressures p_m and p_v varying with respect to $\Delta\pi = \pi_v - \pi_m$. Increasing $\Delta\pi$ means increasing the concentration difference between the interstitial space and the blood vessels, and consequently the increase of the fluid flow from Ω_m to Ω_v.

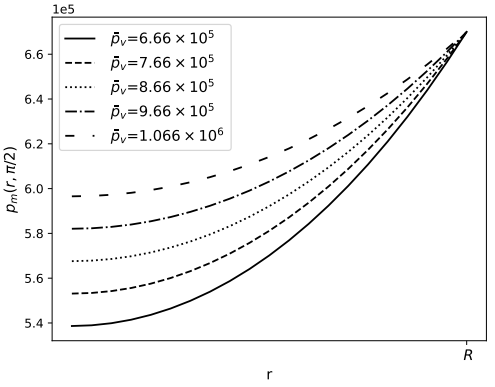

Figure 6. The variation of p_m in mPa at $\theta = \pi/2$, for some values of the blood vessel pressure $\bar{p}_v$ in mPa, with $\pi_v - \pi_m = 1.02 \times 10^6$ mPa, $L_p = 5.475 \times 10^{-10} \frac{\text{mm}}{\text{s mPa}}$, $\bar{p}_m = 6.7 \times 10^5$ mPa and the parameters in Table 2.

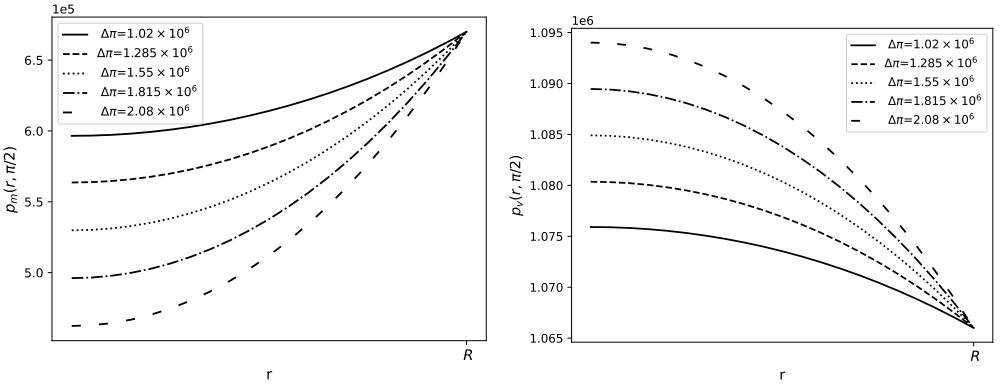

Figure 7. The variation of p_m and p_v in mPa at $\theta = \pi/2$, for some values of the oncotic pressure difference $\Delta\pi = \pi_v - \pi_m$ in mPa, with $\bar{p}_v = 1.066 \times 10^6$ mPa, $L_p = 5.475 \times 10^{-10} \frac{\text{mm}}{\text{s mPa}}$, $\bar{p}_m = 6.7 \times 10^5$ mPa and the parameters in Table 2.

The strength of the explicit solution we found in Section 5 is to take into account the variation with respect to θ of the boundary condition $\bar{p}_m$ to mimic the pressure distribution in the SCS. Unfortunately, as far as we know, there are no precise physiological data available for the pressure distribution in the SCS. Hence, inspired by [15], we take a linear variation of the pressure along the θ coordinate between the values $\bar{p}_{m,max} = 3.9$ mmHg $\approx 5.2 \times 10^5$ mPa and $\bar{p}_{m,min} = 3$ mmHg $\approx 4 \times 10^5$ mPa; these values are taken from the resulting pressure in [22]. Hence we can write:

$$\bar{p}_m(\zeta) = \bar{p}_{m,min} + \frac{\zeta + 1}{2}(\bar{p}_{m,max} - \bar{p}_{m,min}). \tag{6.2}$$

Given this boundary condition, if we use the physiological values used in [22] ($\sigma = 0.88$ and $\pi_v - \pi_m = 1.02 \times 10^6$ mPa), we have an inversion of the flow at $\approx 1.4 \times 10^6$ mPa ≈ 10.5 mmHg, the same found in [22]. We can see this behavior in Figure 8.

In Figure 9 we show the interstitial pressure distribution in the whole domain (recalling that we assume axisymmetry) varying the hydraulic conductivity of the blood vessel walls L_p. As we can see, we have that the position and the value of the minimum of the pressure vary with respect to L_p; as L_p increases, the minimum of the pressure decreases (see Figure 5) and moves towards the center of the node. This is due to a combination of the pressure variation given by

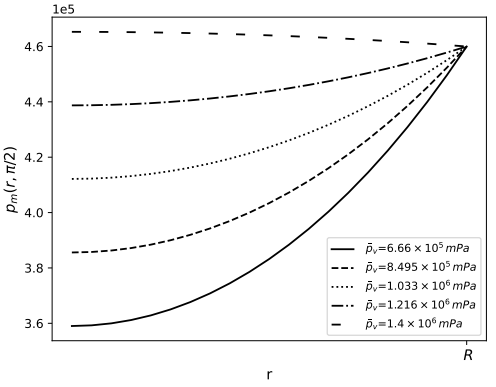

Figure 8. The variation of p_m in mPa at $\theta = \pi/2$, for some values of the mean blood vessel pressure $\bar{p}_v$ in mPa, with $\pi_v - \pi_m = 1.02 \times 10^6$ mPa, $L_p = 5.475 \times 10^{-10} \frac{\text{mm}}{\text{s mPa}}$, the boundary conditions (6.2) and the parameters in Table 2.

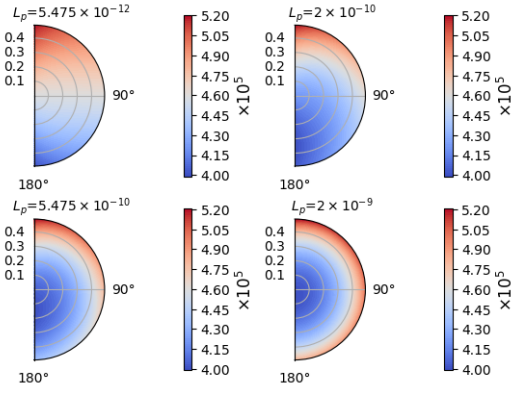

Figure 9. The variation of p_m in mPa in all the domain, for some values of L_p, with $\pi_v - \pi_m = 1.02 \times 10^6$ mPa, $\bar{p}_v = 6.66 \times 10^6$ mPa, the boundary conditions (6.2) and the parameters in Table 2.

the boundary conditions (6.2) and the fluid exchange between phases. These results confirm that the θ dependence in our explicit solution is essential to describe the fluid motion and the pressure distribution inside a lymph node. The value of the minimum pressure is related to a sink term due to the blood vessel's drainage function; here we have that the blood vessel's effect is less relevant with respect to the one found in [22], but the behavior is the same. This is in line with the results of [22], because the permeability that we obtain with our multiscale formulation is bigger than the one used by them.

In Figure 10 we can see the interstitial pressure distribution in the whole domain varying the blood vessel pressure $\bar{p}_v$. As we can see, we have that increasing $\bar{p}_v$ increases the minimum of the pressure p_m and moves the minimum from the center to the lower part ($\zeta = -1$ where we have the minimum in equation (6.2)) of the node. This behavior is the opposite of what we have in Figure 9, in accordance with the results found in Figures 5 and 6.

As we mentioned before, we can choose as boundary condition $\bar{p}_m(\zeta)$ what we want; hence we can choose the more complicated pressure distribution found with the stream function approach

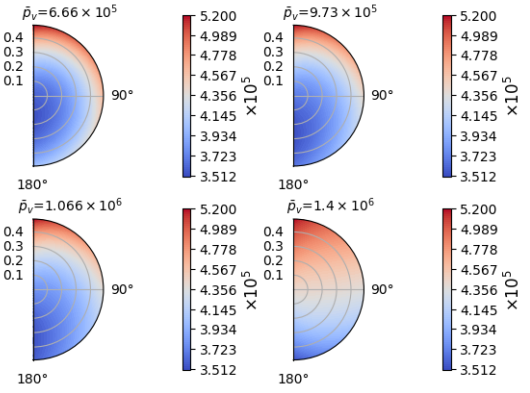

Figure 10. The variation of p_m in mPa in all the domain, for some values of $\bar{p}_v$ in mPa, with $\pi_v - \pi_m = 1.02 \times 10^6$ mPa, $L_p = 5.475 \times 10^{-10} \frac{\text{mm}}{\text{s mPa}}$ the boundary conditions (6.2) and the parameters in Table 2.

in the steady case (see [53] for more details):

$$\bar{p}_m(R,\zeta) = C_{\text{steady}} - \mu \sum_{n=1}^{\infty} \left[\frac{2(2(n+1)+1)}{n} C_n^s R^n + \frac{2(2(n+1)-3)}{n+1} D_n^s R^{-n-1} \right] P_n(\zeta) \quad (6.3)$$

where the constants C_{steady}, C_n^s and D_n^s are calculated in [32] in a steady case without fluid-exchange (div-free solution), where we fix the pressure at one point $\bar{p}_m(R_2,-1) = 6.7 \times 10^5$ mPa and with an inlet and outlet boundary condition defined in the domain $[-1,-1+\zeta_0]$ (outlet condition) and $[1-\zeta_0,1]$ (inlet condition), where $\zeta_0 = \cos\left[\arcsin\left(\frac{R_{LV}}{\sqrt{R_{LV}^2+R_2^2}}\right)\right] = \frac{R_2}{\sqrt{R_{LV}^2+R_2^2}}$, $R_{LV} = 0.04$ mm and $R_2 = 0.5$ mm. The boundary pressure distribution is plotted in Figure 11. We can see that we have a fast increment of pressure near the inlet boundary condition (and a fast decrement near the outlet boundary condition). With these boundary conditions and the parameters $\bar{p}_v = 1.06 \times 10^6$ mPa, $\pi_v - \pi_m = 1.02 \times 10^6$ mPa and $L_p = 5.475 \times 10^{-11} \frac{\text{mm}}{\text{s mPa}}$ we obtain the pressure and the velocity distribution shown in Figure 12. Varying the parameters that regulate the fluid exchange, we obtain the same behavior obtained above. As we can see, we have a pressure distribution similar to those found earlier, but we have a higher (lower) pressure distribution near the inlet (outlet), and we have the same behavior for the velocity magnitude. In this case, we have an inversion of flow with the mean blood vessels pressure $\bar{p}_v \approx 1.53 \times 10^6$ mPa ≈ 11.476 mmHg, similar to the one found with the constant value $\bar{p}_m \approx 6.7 \times 10^5$ mPa. The pressure values found here are in range with the ones measured in [52] and found in [32]. In this case, instead of observing a pressure gradient that varies from a high-pressure region near the inlet to a low-pressure region near the outlet, we find that the low-pressure zone is closer to the center of the LC. This particular region experiences reduced pressure due to the exchange of fluids between lymph and blood vessels, and this phenomenon is represented by a sink term. Due to this, we have that lymph moves toward the low-pressure zone in the center of the node, and we can see this from the velocity plot in Figure 12. Moreover, the velocity behavior is very similar to the one found in [22], although the velocities found here are slightly higher: this is due to the fact that we used a higher L_p than the one used by them and because we found a higher hydraulic conductivity.

Conclusions

In this paper, we have proposed a macroscopic model using the asymptotic homogenization technique resulting from the starting equations (1.1)-(1.2) and the interface condition (1.3), which account for blood transcapillary exchange across the vessels walls, under the assumption of local

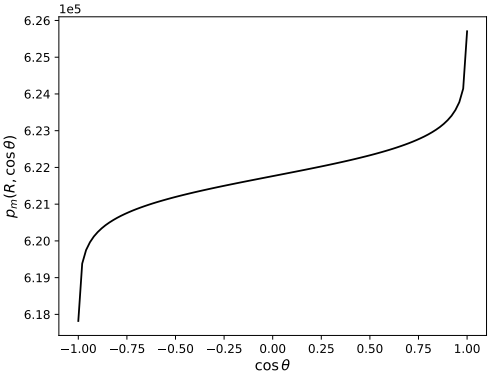

Figure 11. The pressure distribution in mPa of equation (6.3) with the values calculated in [32].

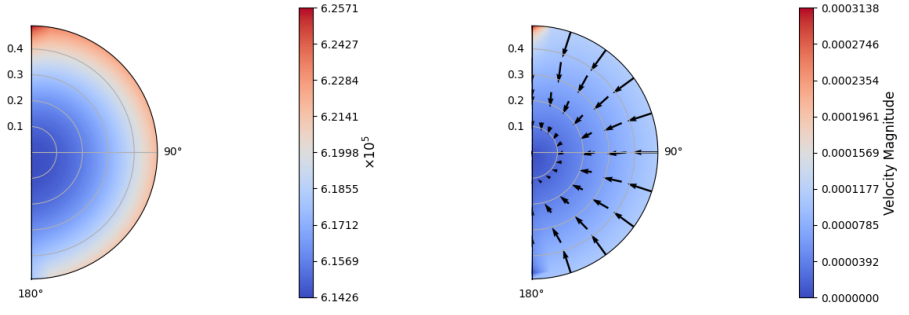

Figure 12. The pressure distribution of p_m (left) in mPa and the velocity distribution (right) in mm/s with boundary conditions (6.3) (values calculated in [32]), $\bar{p}_v = 1.06 \times 10^6$ mPa, $\pi_v - \pi_m = 1.02 \times 10^6$ mPa and $L_p = 5.475 \times 10^{-11} \frac{\text{mm}}{\text{s mPa}}$.

periodicity and macroscopic uniformity in a steady setting. Our starting point is the Darcy/Darcy-Brinkman equation, so we have considered the pore structure already smoothed out, and that simplifies the model because we do not need precise information about the microscale geometry (this information is encoded in the hydraulic conductivity $\hat{\boldsymbol{K}}_\gamma$, $\gamma = m, v$). After that, in Section 4 we have analyzed in detail the differences between using Darcy, Darcy-Brinkman, or Stokes as our starting point, and we have found that the Darcy-Brinkman equation has a Darcy-Stokes duality behavior depending on the value of the permeability (and the relevance of the Laplace operator). Although it is less theoretically justified than the Darcy equation, the Darcy-Brinkman equation is a valid starting point for our multiscale formulation since we have a Stokes-like structure of the differential equation, which allow us to specify in more detail the boundary condition without the need for a precise structure of the microscale, which is described by the permeability parameter (that in most cases is easier to obtain). Moreover, the coupling between the Darcy and Darcy-Brinkman equation has allowed the separation of the cell problem into two distinct phases, one involving the blood vessels and the other involving the FRC network so that we could solve the cell problems in the two domains separately.

After this model analysis, in Section 5 we have found the macroscopic explicit solution of the resulting equation of the proposed model (described in Section 3) in a spherical domain (under certainly simplified hypothesis) in terms of Bessel and Legendre polynomials. Then, in Section 6

we have applied this explicit solution to an idealized spherical lymph node using physiological data from the literature; our multiscale formulation of the problem has allowed us to study the fluid behavior in the interstitial space and in the blood vessels within the node, allowing us to study the interaction and the fluid exchange between these two phases in more detail. We have mainly focused on the porous part of the lymph node (the LC) and on the fluid exchange between the interstitial space of the lymph node and the blood vessels, which are only in this part of the node [22–24]; despite the blood vessel pressure being higher than the interstitial pressure of the node, we have that the blood vessels have a higher concentration of protein too, and this leads to the fact that the lymph goes from the node to the blood circulation, making the lymph nodes important in the fluid regulation within the lymphatic system [21]. We have analyzed how the parameters affect the fluid absorption and the pressure (*i.e.* the velocity) with different boundary pressure, and the behavior of the results is in line with those found in the literature [22,42,47,48, 52].

The current work is open for improvements. First of all, in this analysis, we have considered only the LC and we have supposed a given pressure of the SCS; in general, we need to couple these two motions.

We have assumed that the multiscale forces vanished when we applied our model to a lymph node for the sake of simplicity. In general, these forces can be relevant, for example when electromagnetic fields are used (see, e.g., [54,55] in the context of cancer hyperthermia) so that the role of inhomogeneous volume loads as considered in [10] should be considered when physiological data become available.

We study the fluid flow in a steady case, but in general, we have a time dependence of the flow given by the time-pulsation of the lymphangion [20,43,56]; it will be of crucial importance to address this aspect in future works [31,32].

Finally, we have proposed to use a spherical geometry for the sake of simplicity and to find an explicit solution, but, in general, the LNs are not characterised by a spherical shape and it is reportedly more similar to an ellipsoid [22,27,28,31]. Assuming that more realistic information concerning the shape, e.g. suggested by medical images, become available, our modelling framework could be in future exploited to compute the macroscale solution of the model numerically in order to formulate physiologically relevant predictions.

Acknowledgements. The authors thank the anonymous reviewers for their comments and suggestions. This work was partially supported by National Group of Mathematical Physics (GNFM-INdAM). RP is partially funded by EPSRC grants EP/S030875/1 and EP/T017899/1.

References

1. Darcy H. 1856 *Les fontaines publiques de la ville de Dijon*. Paris: Victor Dalmont.
2. Rajagopal KR. 2007 On a hierarchy of approximate models for flows of incompressible fluids through porous solids. *Mathematical Models and Methods in Applied Sciences* **17**, 215–252.
3. Hornung U. 1997 *Homogenization and Porous Media*. Springer Science+Business Media New York: Springer.
4. Gerisch A, Penta R, Lang J. 2018 *Multiscale Models in Mechano and Tumor Biology*. Gewerbestrasse 11, 6330 Cham, Switzerland: Springer.
5. Brinkman H. 1949 A calculation of the viscous force exerted by a flowing fluid on a dense swarm of particles. *Applied Scientific Research* **A1**, 27–34.
6. Marusic-Paloka E, Pazanin I, Marusic S. 2012 Comparison between Darcy and Brinkman laws in a fracture. *Applied Mathematics and Computation* **218**, 7538–7545.
7. Naele G, Nader W. 1974 Practical Significance of Brinkman's Extension of Darcy's Law: Coupled Parallel Flows within a Channel and a Bounding Porous Medium. *The Canadian lournal of Chemical Engineering* **52**, 475–478.
8. Auriault JL, Geindreau C, Boutin C. 2005 Filtration Law in Porous Media with Poor Separation of Scales. *Transport in Porous Media* **60**, 89–108.
9. Lèvy T. 1983 Fluid flow through an array of fixed particles. *International Journal of Engineering Science* **21**, 11–23.

10. Penta R, Ramírez-Torres AD, Merodio J, Rodríguez-Ramos R. 2020 Effective governing equations for heterogenous porous media subject to inhomogeneous body forces. *Mathematics in Engineering* **3**, 1–17.
11. O'Melia MJ, Lund AW, Thomas SN. 2019 The biophysics of lymphatic transport: Engineering tools and immunological consequences. *Iscience* **22**, 28–43.
12. Arasa J, Collado-Diaz V, Halin C. 2021 Structure and immune function of afferent lymphatics and their mechanistic contribution to dendritic cell and T cell trafficking. *Cells* **10**, 1269.
13. Novkovic M, Onder L, Bocharov G, Ludewig B. 2020 Topological structure and robustness of the lymph node conduit system. *Cell Reports* **30**, 893–904.
14. Roozendaal R, Mebius RE, Kraal G. 2008 The conduit system of the lymph node. *International immunology* **20**, 1483–1487.
15. Grebennikov D, Van Loon R, Novkovic M, Onder L, Savinkov R, Sazonov I, Tretyakova R, Watson DJ, Bocharov G. 2016 Critical issues in modelling lymph node physiology. *Computation* **5**, 3.
16. Savinkov R, Kislitsyn A, Watson DJ, van Loon R, Sazonov I, Novkovic M, Onder L, Bocharov G. 2017 Data-driven modelling of the FRC network for studying the fluid flow in the conduit system. *Engineering Applications of Artificial Intelligence* **62**, 341–349. (10.1016/j.engappai.2016.10.007)
17. Apoorva F, Loiben AM, Shah SB, Purwada A, Fontan L, Goldstein R, Kirby BJ, Melnick AM, Cosgrove BD, Singh A. 2018 How biophysical forces regulate human B cell lymphomas. *Cell reports* **23**, 499–511. (10.1016/j.celrep.2018.03.069)
18. Birmingham KG, O'Melia MJ, Bordy S, Aguilar DR, El-Reyas B, Lesinski G, Thomas SN. 2020 Lymph node subcapsular sinus microenvironment-on-a-chip modeling shear flow relevant to lymphatic metastasis and immune cell homing. *Iscience* **23**, 101751.
19. Permana AD, Nainu F, Moffatt K, Larrañeta E, Donnelly RF. 2021 Recent advances in combination of microneedles and nanomedicines for lymphatic targeted drug delivery. *Wiley Interdisciplinary Reviews: Nanomedicine and Nanobiotechnology* **13**, e1690.
20. Moore Jr JE, Bertram CD. 2018 Lymphatic system flows. *Annual review of fluid mechanics* **50**, 459–482.
21. Tobbia D, Semple J, Baker A, Dumont D, Semple A, Johnston M. 2009 Lymphedema development and lymphatic function following lymph node excision in sheep. *Journal of vascular research* **46**, 426–434.
22. Jafarnejad M, Woodruff MC, Zawieja DC, Carroll MC, Moore Jr J. 2015 Modeling lymph flow and fluid exchange with blood vessels in lymph nodes. *Lymphatic research and biology* **13**, 234–247.
23. Jafarnejad M, Ismail AZ, Duarte D, Vyas C, Ghahramani A, Zawieja, D. C. Lo Celso C, Poologasundarampillai G, Moore Jr. JE. 2019 Quantification of the Whole Lymph Node Vasculature Based on Tomography of the Vessel Corrosion Casts. *Nature Scientific Reports* **9**.
24. Kelch ID, Bogle G, Sands GB, Phillips ARJ, LeGrice IJ, Dunbar PR. 2015 Organ-wide 3D-imaging and topological analysis of the continuous microvascular network in a murine lymph node. *Nature Scientific Reports* **16**.
25. Novkovic M, Onder L, Cheng HW, Bocharov G, Ludewig B. 2018 Integrative computational modeling of the lymph node stromal cell landscape. *Frontiers in Immunology* p. 2428.
26. Shanti A, Teo J, Stefanini C. 2018 In vitro immune organs-on-chip for drug development: a review. *Pharmaceutics* **10**, 278.
27. Cooper LJ, Heppell JP, Clough GF, Ganapathisubramani B, Roose T. 2016 An image-based model of fluid flow through lymph nodes. *Bulletin of mathematical biology* **78**, 52–71.
28. Cooper L, Zeller-Plumhoff B, Clough G, Ganapathisubramani B, Roose T. 2018 Using high resolution X-ray computed tomography to create an image based model of a lymph node. *Journal of Theoretical Biology* **449**, 73–82.
29. Shanti A, Samara B, Abdullah A, Hallfors N, Accoto D, Sapudom J, Alatoom A, Teo J, Danti S, Stefanini C. 2020 Multi-compartment 3D-cultured organ-on-a-chip: towards a biomimetic lymph node for drug development. *Pharmaceutics* **12**, 464.
30. Tretiakova R, Setukha A, Savinkov R, Grebennikov D, Bocharov G. 2021 Mathematical Modeling of Lymph Node Drainage Function by Neural Network. *Mathematics* **9**, 3093.
31. Giantesio G, Girelli A, Musesti A. 2021 A model of the pulsatile fluid flow in the lymph node. *Mechanics Research Communications* **116**, 103743.
32. Giantesio G, Girelli A, Musesti A. 2022 A mathematical description of the flow in a spherical lymph node. *Bulletin of Mathematical Biology* **84**.

33. Discacciati M, Quarteroni A. 2009 Navier-Stokes/Darcy Coupling: Modeling, Analysis, and Numerical Approximation. *Revista Matemática Complutense* **22**, 315–426.
34. Waniewski J. 2006 Mathematical modeling of fluid and solute transport in hemodialysis and peritoneal dialysis. *Journal of Membrane Sciences* **274**, 24–37.
35. Formaggia L, Quarteroni A, Veneziani A. 2009 *Cardiovascular Mathematics: Modeling and Simulation of the Circulatory System*. Milano: Springer-Verlag.
36. Penta R, Ambrosi D, Quarteroni A. 2015 Multiscale homogenization for fluid and drug transport in vascularized malignant tissues. *Mathematical Models and Methods in Applied Sciences* **25**, 79–108.
37. Mascheroni P, Penta R. 2017 The role of the microvascular network structure on diffusion and consumption of anticancer drugs. *International journal for numerical methods in biomedical engineering* **33**, e2857.
38. Shipley RJ, Chapman SJ. 2010 Multiscale modelling of fluid and drug transport in vascular tumours. *Bulletin of mathematical biology* **72**, 1464–1491.
39. Penta R, Ambrosi D. 2015 The role of the microvascular tortuosity in tumor transport phenomena. *Journal of Theoretical Biology* **364**, 80–97.
40. Abramowitz M, Stegun IA. 1964 *Handbook of mathematical functions with formulas, graphs, and mathematical tables* vol. 55. Washington, D.C.: US Government printing office.
41. Ohtani O, Ohtani Y. 2008 Structure and function of rat lymph nodes. *Archives of histology and cytology* **71**, 69–76.
42. Adair TH, Guyton AC. 1985 Modification of lymph by lymph nodes. III. Effect of increased lymph hydrostatic pressure. *American Journal of Physiology-Heart and Circulatory Physiology* **249**, H777–H782.
43. Bertram C, Macaskill C, Davis M, Moore J. 2017 Valve-related modes of pump failure in collecting lymphatics: numerical and experimental investigation. *Biomechanics and modeling in mechanobiology* **16**, 1987–2003.
44. Ochoa-Tapia JA, Whitaker S. 1995a Momentum transfer at the boundary between a porous medium and a homogeneous fluid I. Theoretical development. *International Journal of Heat and Mass Transfer* **38**, 2635–2646.
45. Ochoa-Tapia JA, Whitaker S. 1995b Momentum transfer at the boundary between a porous medium and a homogeneous fluid II. Comparison with experiment. *International Journal of Heat and Mass Transfer* **38**, 2647–2655.
46. Tan H, Pillai KM. 2009 Finite element implementation of stress-jump and stress-continuity conditions at porous-medium, clear-fluid interface. *Computers & Fluids* **38**, 1118–1131.
47. Adair TH, Moffatt DS, Paulsen AW, Guyton AC. 1982 Quantitation of changes in lymph protein concentration during lymph node transit. *American Journal of Physiology-Heart and Circulatory Physiology* **243**, H351–H359.
48. Adair TH, Guyton AC. 1983 Modification of lymph by lymph nodes. II. Effect of increased lymph node venous blood pressure. *American Journal of Physiology-Heart and Circulatory Physiology* **245**, H616–H622.
49. Stohrer M, Boucher Y, Stangassinger M, Jain RK. 2000 Oncotic Pressure in Solid Tumors Is Elevated. *Cancer Research* **60**, 4251–4255.
50. Kozeny J. 1927 Ueber kapillare Leitung des Wassers im Boden. *Sitzungsber Akad. Wiss.* **136**, 271–306.
51. Carman PC. 1997 Fluid flow through granular beds. *Chemical Engineering Research and Design* **75**, S32–S48.
52. Bouta EM, Wood RW, Brown EB, Rahimi H, Ritchlin CT, Schwarz EM. 2014 In vivo quantification of lymph viscosity and pressure in lymphatic vessels and draining lymph nodes of arthritic joints in mice. *The Journal of physiology* **592**, 1213–1223.
53. Happel J, Brenner H. 1983 *Low Reynolds number hydrodynamics: with special applications to particulate media*. The Hague: Martinus Nijhoff Publishers.
54. Al Sariri T, Penta R. 2022 Multi-scale modelling of nanoparticle delivery and heat transport in vascularised tumours. *Mathematical Medicine and Biology: A Journal of the IMA* **39**, 332–367.
55. Al Sariri T, Simitev RD, Penta R. 2023 Optimal heat transport induced by magnetic nanoparticle delivery in vascularised tumours. *Journal of Theoretical Biology* **561**, 111372.
56. Bertram C, Macaskill C, Moore J. 2019 Inhibition of contraction strength and frequency by wall shear stress in a single-lymphangion model. *Journal of biomechanical engineering* **141**.